UNIVERSITÀ
DEGLI STUDI
FIRENZE

Università degli Studi di Firenze
Dipartimento di Ingegneria dell'Informazione (DINFO)
Corso di Dottorato in Ingegneria dell'Informazione
Curriculum: Telecomunicazioni

Advanced methods for volumetric interpolation and multimodal fusion of tomographic sequences with application to 3D reconstruction in biomedicine

Candidate
Chiara Santarelli

Supervisors
Prof. Fabrizio Argenti

Prof. Luciano Alparone

Prof.ssa Monica Carfagni

PhD Coordinator
Prof. Fabio Schoen

ciclo XXXIII, 2017-2020
Settore Scientifico Disciplinare ING-INF/03

Università degli Studi di Firenze, Dipartimento di Ingegneria dell'Informazione (DINFO).

To my mother Ornella,
who taught me,
with great humility and wisdom,
the essence of life.

Acknowledgments

My acknowledgments to my supervisors, Professor Fabrizio Argenti, Professor Luciano Alparone and Professor Monica Carfagni, with their efforts and contributions gave me the opportunity to enter the extraordinary world of research. Thanks, also, to my colleagues for their help during this professional path. Special thanks to my family, especially my uncle Nedo, my greatest support and guide.

Abstract

Recently, anatomical 3D models, thanks also to the increased diffusion of 3D printing technologies, have been successfully introduced in the clinical field as innovative tools to support the medical team in several tasks. Advances in 3D technology now provide a realistic representation of complex anatomies that can be used as an aid for diagnosis, surgical planning and training. In general, 3D reconstructions are more accurate when they are the outcome of the processing of high-resolution image sequences. On the other hand, if a sequence is characterized by few tomographic sections, only a coarse reconstruction is achievable and the artifacts that are produced impair the usefulness as a tool to support the physician. The study carried out during this thesis work has two objectives. The first is to provide axial interpolation methods that, applied to low-resolution sequences, allow a refined 3D reconstruction of the anatomical model to be obtained. The methods are inspired by compensated frame interpolation techniques (MCFI) developed for video processing applications and produce an estimate of the displacement vector field (DVF). The DVF is then processed and used to estimate intermediate ones. The performance of the proposed methods has been quantitatively assessed using sequences with simulated axial low resolution. The experimental results show that the proposed methods allow an effective sliced interpolation and the 3D models obtained clearly benefit from the increased axial resolution. The second objective is studying image fusion methods specific for biomedical images obtained from different acquisition methods, also termed as multimodal image fusion. More specifically, in this thesis magnetic resonance imaging (MRI) and magnetic resonance elastography (MRE) sequences have been taken into account. The objective of the processing is achieving a fused image containing the structural information from the MRI and the mechanical (tissue stiffness) information from the MRE. The proposed method is based on multiresolution analysis (MRA). The fused MRE image is obtained by adding the geometric details, extracted from the MRI, after being modulated by a suitable injection gain. This gain is based on a correlation coefficient between the two images. The results show its effectiveness in providing in an unique image both the geometric information and elastic properties of the investigated tissues.

Contents

List of Figures

List of Tables

Acronyms

ABS Acrylonitrile Butadiene Styrene. 43

ADC Apparent Diffusion Coefficient. 14

AIDE Algebraic Inversion of Differential Equation. 25

AM Additive Manufacturing. 1

CAD Computer Aided Design. 36

CT Computed Tomography. 2

DICOM Digital Imaging and COmunications in Medicine. 45

DTI Diffusion Tensor Imaging. 15

DVF Displacement Vector Field. 57

DWI Diffusion Weighting Imaging. 13

FDM Fused Deposition Modeling. 47

fMRI Functional Magnetic Resonance Imaging. 14

HU Hunsfield Unit. 8

MCFI Motion Compensated Frame Interpolation. 55

ME Motion Estimation. 55

MRE Magnetic Resonance Elastography. 2, 18

MRI Magnetic Resonance Imaging. 2

MV Motion Vector. 58

OF Optical Flow. 56

PD Proton Density. 11

PEG Polyethylene Glycol. 44

PET Positron Emission Tomography. 15

PHY Phytagel. 44

PLA Polylactic Acid. 43

PS Physical Simulator. 36

PVA Polyvinyl Alcohol. 44

PWI Perfusion Weighted Imaging. 14

RF Radio Frequency. 10

ROI Region Of Interest. 41

SE spin-echo. 12

TE echo time. 12

TR repetition time. 12

VS Virtual Simulator. 36

Chapter 1

Introduction

In the recent years, 3D modeling has been successfully introduced in the clinical field as an innovative tool to support the medical team; this has been made possible also thanks to the wider and wider diffusion of 3D printing technologies. 3D printing is a manufacturing technique that enables objects to be realized from digital data by using specific software and a printer that adds layer upon layer of material to create the shape of the desired object. This technology is defined as Additive Manufacturing (AM). Through 3D printing it is possible to make objects of any kind using a wide range of materials such as thermoplastics, polymers, metal and so on. In the biomedical field, 3D printing has been present since the early 2000s, when the technology was first used for the creation of dental implants and customized prosthetics. Since then, medical applications of 3D printing have evolved considerably and current medical uses can be organized into two categories: organ and tissue manufacturing and creation of prostheses, implants and anatomical models. The technology of 3D reconstruction and printing allows solutions customized on patients' needs to studied and realized. It can also be widely applied in medical diagnosis and surgical planning, since it represents a valuable help for surgeons in pre-operative and post-operative phases. Thanks to the three-dimensional reconstruction of anatomical districts, biomodels are created that faithfully replicate the pathology of the patient and serve as a basis for preventive study of the surgery. Difficulties, anatomical conditions, different depths and lengths of surgical instruments and possible instrumentation can be foreseen in advance, with the undisputed advantage of having greater clarity, greater safety and speed of execution. In addition, in the post-

operative phase, it allows the correct execution of the operation to be verified and, in particular cases, defects to be detected and possible corrections to be made. The advantage of biomodels is to go beyond traditional radiology, integrating the virtual reality of 3D radiology with the physical reality of a three-dimensional object on which you can perform a real surgery in the laboratory or operating room. A further advantage of 3D models is the natural and immediate perception of the case under consideration, as well as an important means of communication both for the patient himself and for the families, which is not feasible with 2D. Through these models you can have a tactile feedback, and this allows a greater understanding and safety by the surgeon with a consequent reduction of surgical errors and operating time. The quality of the 3D model depends on the axial resolution of the sequence used during the 3D reconstruction process. On the other hand, a very coarse reconstruction characterised by artefacts is obtained if the sequence consists of only a few tomographic sections. In this case we refer to sequences with low axial resolution. This is the case, for example, of Computed Tomography (CT) scans performed on neonatal patients suffering from craniosynostosis. To solve this problem, axial interpolation can be considered to generate intermediate slices from two adjacent ones of the same sequence in order to increase the resolution in the axial direction. Another example of a low axial resolution sequence is Magnetic Resonance Elastography (MRE), a diagnostic tool to determine certain mechanical properties of tissues in vivo. The mechanical characterization of human organs is of great impact on medical practice, particularly for diagnosis, planning and surgical training, for tissue engineering and trauma research. Classical imaging methods, such as CT and Magnetic Resonance Imaging (MRI), allow an anatomical structure to be visualized and its functionality and the presence of pathologies to be verified, even though information about the mechanical properties of tissues can not be achieved. Measuring the elastic properties of tissues is of great interest since it is assumed that the diseased anatomical parts have different mechanical properties than healthy ones (a greater rigidity of tissues, for example, may be related to a pathological state), so that MRE becomes a tool to discriminate different physiological tissues. Nevertheless, MRE data do not provide any information about anatomical structures. The fusion of MRI and MRE images would result in a final image, in which both the geometric content of the MRI and the elasticity information of the MRE are present, enabling physicians to perform a more accurate and complete investigation

of the entire anatomical part of interest. This thesis work presents methods for volumetric interpolation and fusion of tomographic sequences with application to 3D reconstruction; after an excursus on the state of the art of the main medical image acquisition techniques, we will analyze the problem of 3D reconstruction of an anatomical model. We will also analyze the aspects of image processing necessary for the reconstruction of geometrically accurate 3D models from image sequences. Finally, the biomedical images fusion process will be examined.

Chapter 2

Biomedical imaging

This chapter provides a brief overview of biomedical images formation and their main acquisition techniques. In the first part of the chapter, the most common and traditional imaging techniques will be described while in the second part a new technique providing a mechanical characterization of tissues will be presented.

2.1 Traditional diagnostic imaging

The term diagnostic imaging or imaging refers to the process of generating medical images used for diagnostic purposes and includes radiology, computed tomography, magnetic resonance imaging, ultrasound, pet and so on. Imaging provides the physician with a very important diagnostic tool in the development of a detailed and accurate clinical picture of the patient and can be integrated with other diagnostic techniques. The various diagnostic imaging techniques use electromagnetic signals produced by a source and measure the interaction between this energy and the organ to be analyzed. The generated signal by the source propagates in space and when it interacts with the organ, a fraction of the energy is reflected backwards, another fraction propagates through the tissues (and eventually beyond) modifying its characteristics in general, and another part of the energy is somehow absorbed by the organ itself. These physical phenomena (reflection, refraction and absorption) vary depending on the type of tissues and on the type of energy and, therefore, the diagnostic technique vary. The first and nowadays simplest technique of medical imaging was introduced about one hundred

years ago and involves the use of electromagnetic waves to generate black and white images where the various tissues are different due to different levels of radiation absorption, the bones that absorb the maximum appear white while the air absorbing the minimum appears black. A significant limitation of this technique is the impossibility to provide a three-dimensional view of the investigated organ. In the following we will analyze the diagnostic techniques mentioned above, focusing on those that allow both a visualization and a reconstruction of the 3D model of the organ of interest.

2.1.1 Computed tomography (CT)

CT is an imaging technique that uses ionizing radiation (X-rays) to scan body and to reproduce body sections of the patient allowing a three-dimensional visualization and processing. The anatomical part of interest can be scanned in two modalities: sequential or volumetric. In the first one, the X-ray tube rotates around the patient making a 360 degrees rotation at the end of which the table moves longitudinally and the next scan is performed. This is done until the end of the scan of the entire volume of interest. In the volumetric mode, the radiant beam describes a helical trajectory around the patient and data acquisition takes place simultaneously with the movement of the table (Figure 2.1). During the scan, the detectors (sensors) measure the radiation transmitted through the patient by providing a map of attenuation of the different tissues which is used to reconstruct a digital image of an axial section (Figure 2.2).

Digital images consist of a pixels that represent the average attenuation value of each voxel which is the unit volume element. The term attenuation indicates the reduction of energy that the X-ray beam undergoes when it passes through the object; the Lambert-Beer law is used to calculate the linear attenuation coefficient, that is

$$\mu = \frac{1}{\Delta x} \ln \frac{I_t}{I_0} \tag{2.1}$$

where I_t represents the transmitted energy, I_0 the incident energy and Δx the thickness of the penetrated tissue. Since the photon beam is heterogeneous, it is necessary to consider the number of photons and consequently the Lambert-Beer equation becomes

$$N_t = N_0 e^{-\mu \Delta x} \tag{2.2}$$

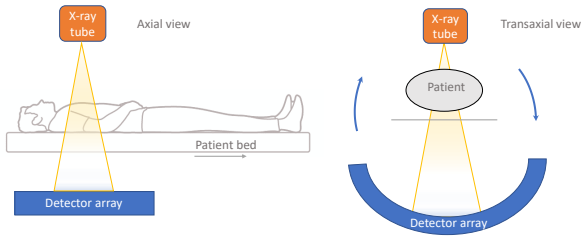

Figure 2.1: Diagram of a CT scanner. The X-ray tube and detector array rotate in the transaxial plane while the patient's bed moves along the axial direction.

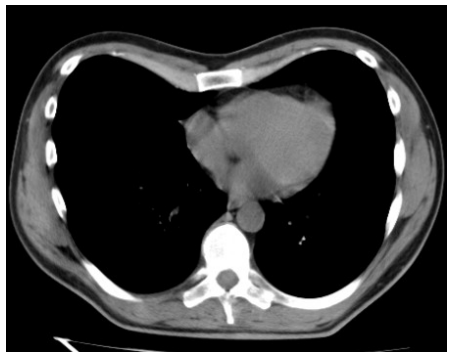

Figure 2.2: Example of axial chest CT images.

where N_t represents the number of transmitted photons and N_0 the number of incident photons. Considering that the body of a patient consists of tissues with different density and each one characterized by a specific attenuation coefficient, the number of photons results to be

$$N_t = N_0 e^{-(\mu_1 ds + \mu_2 ds + ...)} \tag{2.3}$$

The CT image is produced on a pixel matrix , where each pixel (or voxel) corresponds to a particular attenuation value that is then transformed into

a proportional gray tonality value. Such value takes the name of Hunsfield Unit (HU) and is defined by the following equation

$$HU = k\frac{\mu_t - \mu_w}{\mu_w} \tag{2.4}$$

where μ_t and μ_w represent the tissue and water attenuation coefficients, respectively, while k is a scale factor. The Hounsfield unit describes the tissue radiodensity and is referred to the water density, which by convention is equal to 0. Table 2.1.1 shows some examples of HU in related to various tissues [6].

TISSUE	HU
Air	- 1000
Lung	- 500
Adipose tissue	- 100 ÷ - 50
Water	0
Cerebrospinal fluid	+ 15
Kidney	+ 30
Blood	+ 30 ÷ + 45
Muscular tissue	+ 10 ÷ + 40
Grey matter	+ 37 ÷ + 45
White matter	+ 20 ÷ + 30
Liver	+ 40 ÷ + 60
Contrast agent	+ 100 ÷ + 300
Bone	+ 400 ÷ + 3000

Table 2.1: HU values for various types of tissue.

In CT examinations organs and tissues may be classified as ***hyperdense*, *hypodense* or *isodense*** in relation to another organ or tissue or the reference water density. As can be seen in Figure 2.3, hyper dense structures such as bones appear white and hypodense substances such as air appear black.

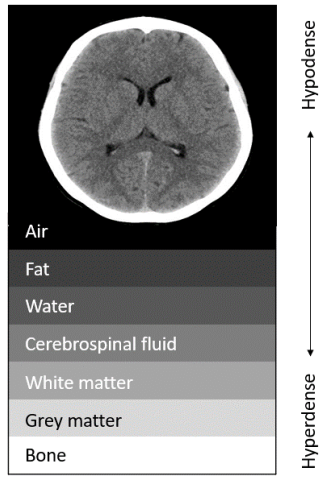

Figure 2.3: Qualitative tissues classification.

2.1.2 Magnetic resonance imaging (MRI)

MRI provides sequences of sections of the body in the form of two-dimensional images in the same manner as CT scans. The content and therefore the information provided are different since this technique exploits the physical phenomenon of Nuclear Magnetic Resonance, according to which some nuclei of elements present in the human body (in particular the hydrogen nucleus) react differently in response to the application of a very intense external magnetic field. This physical phenomenon occurs due to the interaction within the human body between this intense magnetic field and electromagnetic waves of appropriate frequency, sent to the patient's body.

Physical principles

When the patient is introduced into an MRI device, hydrogen ions, which have an odd number of protons in the nucleus and then acting like a small magnet, are oriented with respect to the static field of the machine (B_0) in only two possible directions, parallel or antiparallel [7]. Parallel protons are prevalent over antiparallel ones thus producing a *resulting magnetization* M, oriented parallel to B_0, and the axis of each proton rotates around the di-

rection of the precession moment. During precession (Figure 2.4) the proton rotation axis rotates describing a cone. The "turns/revolution" number that

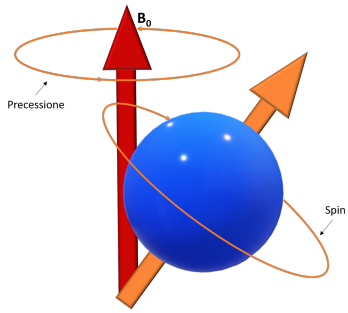

Figure 2.4: Precession phenomenon.

the proton completes in a second, around the field force lines, is indicated by the term frequency which depends both on the type of atom and the force of the applied magnetic field, according to Larmor's law:

$$\omega = \gamma \frac{B_0}{2\pi} \tag{2.5}$$

where ω represents the frequency (MHz), γ the Larmor constant (MHz / T) and B_0 the intensity magnetic field (T). Larmor's constant for hydrogen nuclei is 42, which means that in the presence of a 1.0 Tesla magnetic field, hydrogen atoms rotate at 42 MHz (42 million of turns/revolution per second). By sending Radio Frequency (RF) pulses, it is possible to interact with the precession system (this phenomenon is called resonance). For this purpose it is, however, necessary to send an impulse that has the same frequency as the Larmor. This mainly determines two aspects:

1. The synchronization of the precession (protons rotate not only at the same frequency but also in a coordinated way) that establishes a new macroscopic magnetization, in the orthogonal plane at B_0, called transverse magnetization.

2. The change of state of some protons from the low energy level (parallel to B_0) to the high energy level (antiparallel to B_0).

After the impulse, the spin will tend to return to the previous energy equilibrium situation, realigning with the main magnetic field and emitting a

radio frequency wave that measured by a receiving antenna is converted into a digital signal. This longitudinal relaxation is also called spin-lattice relaxation, and the time constant describing it is named T1. T2 (transverse relaxation time) is the time constant which determines the rate at which excited protons reach equilibrium or go out of phase with each other. It is also possible to measure how many hydrogen protons are present in the single voxel, called Proton Density (PD). T1, T2 and proton density are, therefore, to be considered as intrinsic tissues characteristics.

Type of MRI images

The image content depends on the hydrogen nuclei concentration in tissues and since hydrogen is present in the human body essentially in the form of water, on the tissue water concentration. For this reason, the information provided by MRI images are different from those of other imaging methods: in fact, based on the particular biochemical composition of different tissues, it is possible to distinguish them. The importance of this examination lies in the fact that it can discriminate, for example, between a tissue of the liver and one of the spleen (which compared to X-rays have the same optical density), or healthy tissue from lesions. In describing most of the MRI sequences reference is made to the tissues or fluids shades of gray in relation to the signal intensity, obtaining the following absolute terms:

- **White** indicates high signal strength
- **Grey** indicates an intermediate signal strength
- **Black** indicates low signal strength

The anomalies are described by their relationship of intensity with a reference structure (brain tissue, CSF etc.). The descriptors used are:

- **Hyperintense**: if an anomaly is bright (white) as shown in Figure 2.5.
- **Isointense**: if an anomaly has the same intensity as a reference structure.
- **Hypointense**: if an anomaly is dark.

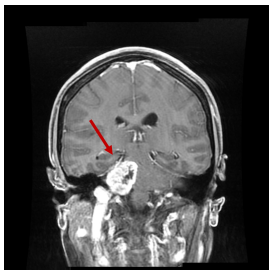

Figure 2.5: Hyperintense lesion example. Image taken from [1]

There are many RF pulse sequences and those currently most commonly used are called "spin-echo (SE)" and "inversion recovery". These sequences offer T1,T2 or PD weighted images by manipulating the repetition time (TR) and echo time (TE) which represent, the time between one RF transmission and the next, and the time between excitation and when the coil is programmed to receive the resulting signal, respectively [8]. Table 2.1.2 classifies the three image types according to TR and TE. Due to the re-

IMAGE	TR	TE
T1	Short	Short
T2	Long	Long
PD	Long	Short

Table 2.2: Echo and repetition time for different types of MRI images.

laxation and phase shift properties (T1, T2) and the proton density value, differentiation between different body tissues is possible in MRI. Tissue contrast is influenced not only by T1, T2 and DP values of specific tissues, but also by differences in magnetic field strength, temperature variations and many other factors [9]. The various types of magnetic resonance imaging are distinguished by the different signal intensities of the tissues and thus the different gray values as shown in Table 2.3. In Figure 2.6 are shown MRI images of the same brain acquired in T1, T2 and PD mode.
Paramagnetic contrast agents are used to improve MRI images and visualize pathologies. They have their strongest effect in T1-weighted images because they mainly alter the T1 relaxation time in the tissues where they have accumulated. The most commonly used contrast agent in MRI are the basic

TISSUE	T1 (Signal strength)	T2 (Signal strength)	PD (Signal strength)
Fluid (urine,CSF,etc..)	Low (black)	High (white)	High (white)
Muscle	Intermediate (gray)	Intermediate (gray)	Intermediate (gray)
Fat	High (white)	Low (black)	High (white)
Grey matter	Intermediate (gray)	Intermediate (gray)	Intermediate (gray)
White matter (respect to gray matter)	Hyperintense (whiteish)	Hypointense (darkish)	Hypointense (darkish)

Table 2.3: Signal intensity of different tissues.

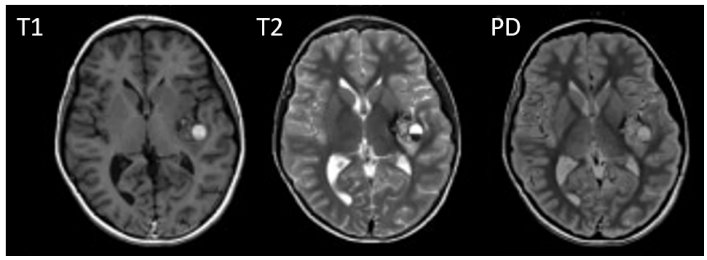

Figure 2.6: MRI of the brain. From left to right T1, T2 and PD images.

gadolinium. Contrast is injected intravenously (usually 5-15 ml) and scans are obtained a few minutes after administration. Pathological tissues (tumors, areas of inflammation or infection) have an accumulation of contrast and therefore appear brighter than the surrounding tissue [10]. It is also possible to obtain images in which the light signal of fat is suppressed. This most commonly occurs in two scenarios: first, after contrast administration to make the tissue to be analyzed more visible, second, if you want to analyze a particular adipose tissue that becomes dark.
The continuous evolution of magnetic resonance imaging systems leads to more advanced and innovative investigation techniques; in the following, some examples are given.

Diffusion
In this case we refer to Diffusion Weighting Imaging (DWI) which is a diffusion-weighted image that shows variations in the mobility of water protons in a biological tissue. In these images, structures with “normal” diffusion are conventionally represented darker, because the resonance signal is

more attenuated, while where the diffusion rate is lower ("restricted"), as in ischemia for example, are represented lighter. The DWI thus allow a qualitative analysis, representing the spatial distribution of the water molecules in a voxel. To be able to talk about quantitative analysis we need to introduce the Apparent Diffusion Coefficient (ADC) maps. These maps are the "negative" of the DWI images, and they allow an analysis of the quantitative diffusion through the identification of physical parameters. Figure 2.7 shows a DWI type image and an ADC type image.

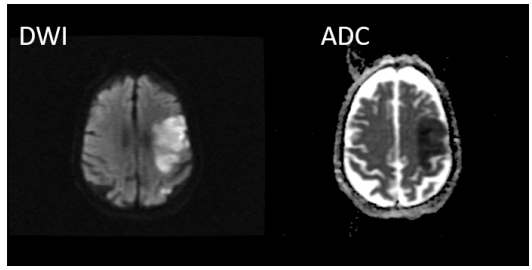

Figure 2.7: Example of DWI type image and ADC type image. Image taken from [1]

Perfusion

Perfusion Weighted Imaging (PWI) sequences allow an evaluation of the cerebral blood flow. Generally, they require the use of a paramagnetic contrast medium, then going to analyze the signal changes obtained during the passage of the same in the vascular bed. In the presence of an "altered" cerebral blood flow, the detected signal will be reduced [11] (Figure 2.8a).

Spectroscopy

Different components interact with the magnetic field of MRI scanners in slightly different ways and the amounts of these components can be quantified in a prescribed region of the tissue. These can be used to help characterize the tissue in the tumor diagnosis or classification [12] (Figure 2.8b).

Functional MRI

Functional Magnetic Resonance Imaging (fMRI) is a technique used to obtain functional information by visualizing cortical activity. With such a method a blood flow small alteration can be detected in response to stimuli

or actions [13] (Figure 2.8c).

Tractography
Magnetic resonance imaging with Diffusion Tensor Imaging (DTI) is a technique that involves the use of an instrument that allows to obtain images based on the analysis of the movement of water molecules present in brain tissue. The resulting data can also be used to three-dimensionally map the white matter, a method that is called tractography (Figure 2.8d).

The figure shows examples of the four types of images described above

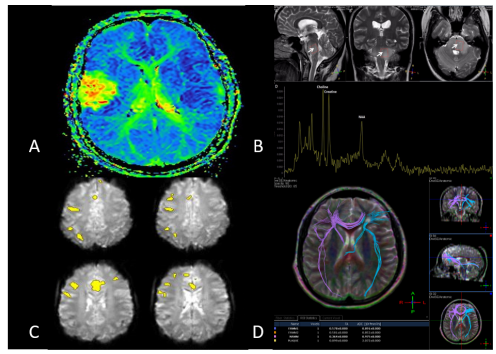

Figure 2.8: Innovative MRI techniques. From A to D example of PWI image, spectroscopy, fMRI image and tractography. Figure A is taken from https://www.mrinnovations.com/pwi. Figures B, C and D are taken from [1]

2.1.3 Positron emission tomography (PET)

Positron Emission Tomography (PET) is a diagnostic imaging method that allows tissues with high metabolic activity (e.g. tumors) to be identified and their size and location to be estimated. The examination is based on the administration of radiopharmaceuticals, characterized by the emission of particles called positrons that allows the radiation emitted by the positrons of the tissues to be detect and processed. The substantial difference with other methods of investigation such as, for example, MRI and CT is that PET can provide quantitative and qualitative information of the tissues under examination. An example of PET images is shown in figure 2.9. With this examination it is possible to detect tumors, Alzheimer's disease, control the

metabolism of the brain and locate the origin of epileptic activity [14].

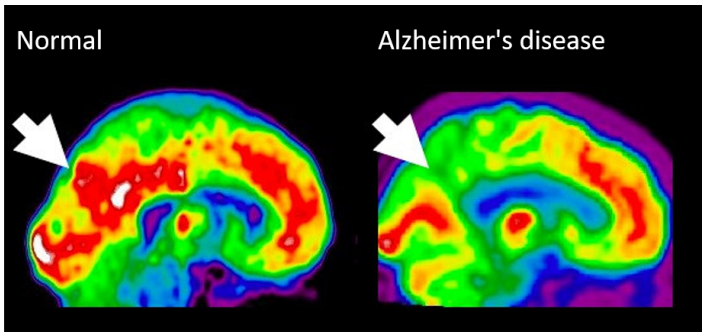

Figure 2.9: PET image of healthy brain (left) and Alzheimer's brain (right).

2.1.4 Ultrasound ecography (UE)

It is a diagnostic imaging method based on the use of high frequency mechanical waves (ultrasound). The physical principle on which it is based is to detect the reflections that ultrasounds undergo in passing through biological tissues. The ultrasounds used are waves generated by a piezoelectric crystal inserted in a probe maintained with the interposition of a special gel in direct contact with the patient's skin. The same probe is able to collect the return signal, which is properly processed by a computer and presented on a monitor. The echo corresponds to the secondary acoustic wave consisting of the portion of the incident ultrasonic beam that returns towards the probe when it crosses an intermediate zone between two mediums that have different acoustic impedance. Acoustic impedance is the product between the medium density and the speed of sound propagation in the medium itself. This method is considered as a basic examination or filter compared to more complex and invasive imaging techniques such as CT and MRI. The ultrasound is, in any case, operator-dependent, as it requires special skills of manual ability and spirit of observation, in addition to image culture and clinical experience. The ultrasound frequencies used for diagnostic purposes are between 1 and 30 MHz and the propagation speed varies depending on the medium density. The echoes produced by ultrasound can be displayed in different ways:

- A-mode (Amplitude mode): was the first display mode; in disuse, it still finds residual applications in the ultrasound of the eye.
- B-mode (Brightness mode): the echoes are represented according to their distance from the source, determined on the basis of the delay with which they return to the probe. An example of this method is represented in figure 2.10 A.
- M-mode or TM-mode (Motion or Time Motion mode): used to display organ movements
- 4D mode: is a 3-dimensional B-Mode ultrasound plus time component (Figure 2.10 B).

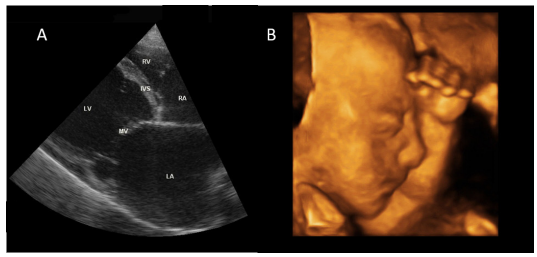

Figure 2.10: Example of UE image. (A) US B-mode; (B) US 4D mode.

2.2 Magnetic resonance Elastography (MRE)

2.2.1 Introduction

Palpation is the most important and immediate clinical method for the diagnosis of diseases, since the pathological processes cause substantial changes in the tissue's mechanical properties, which are therefore of different consistency. The first consideration regarding these distinctions date back to 400 B.C. in the text "the book of predictions" which was made explicit by Hippocrates. The "elastic" tissues have since been considered healthy in the medical field, while the "rigid" ones are associated with pathological processes such as chronic inflammation or cancer. Palpation, however, has its limits as a diagnostic tool because it is subjective and unable to classify the various components of the tissue, thereby providing only qualitative analysis.

In 1995 a new imaging technique named Magnetic Resonance Elastography (MRE) was developed to address these issues. This method is proposed as a non invasive technique able to quantify the viscoelastic properties of tissues in vivo, i.e. the ability of tissues to undergo deformation when subjected to pressure stress and then return to their original shape. The basic concept behind elastography involves three stages: generation of stress in the tissue of the target, study of tissue deformation, and characterization of the tissue by dynamic stress-deformation. Stress is defined as applied force per unit area in materials science, while deformation is defined as tissue displacement per unit sample length. The elastic modulus, a physical parameter representing the intrinsic rigidity of the tissue, is the slope of the tension-deformation curve [15] (Figure 2.11).

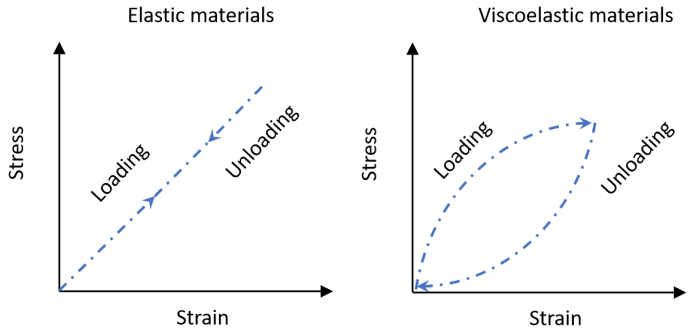

Figure 2.11: Stress-strain curve for elastic and viscoelastic materials.

Depending on the type of stress detected, the elastic modulus is reported as Young modulus **E**, which provides information on the material's rigidity at longitudinal stress, shear modulus **G** representing the material's rigidity at shear stress and mass modulus **K** representing the ratio between volumetric stress and volumetric deformation. The SI unit for the elastic modulus is expressed in kilopascals (KPa) where 1 kPa = 1 kN/m^2 and the ratio between the various elastic magnitudes is defined by the relations:

$$G = \frac{E}{2(1+v)} \tag{2.6}$$

$$K = \frac{E}{3(1-2v)} \tag{2.7}$$

where v represents Poisson's ratio between G and E, and is expressed as:

$$v = \frac{E}{2G} - 1 \tag{2.8}$$

2.2.2 Operating principal

In conjunction with a magnetic resonance imaging technique, MRE uses the propagation of mechanical shear waves (Gamma, 20-200 Hz) to probe the mechanical properties of the tissues. The movement of nuclear rotations (spin) in the presence of a magnetic field gradient induces a phase shift in an MRI signal, provided by

$$\varphi(\tau) = \gamma \int_0^\tau \vec{G}_r(t) \cdot \vec{r}(t) dt \tag{2.9}$$

where $G_r(t)$ is the magnetic field gradient, $r(t)$ is the position vector of nuclear rotations and φ is the gyromagnetic ratio characteristic of the nuclei under examination [16]. Equation 2.9 indicates that the phase shift observed in the received MRI signal is a function of the gradient vector and position vector. If we consider the specific case of the harmonic acoustic wave propagation, the spins undergo a simple known harmonic motion with respect to their average position. Therefore, you could consider the gradient vector $G_r(t)$ as one of a set of basic functions used to estimate the harmonic components of the position vector $r(t)$. First we consider the function $G_r(t)$ truncated in time by the function $w(t)$, so that equation 2.9 becomes

$$\varphi(\tau) = \gamma \int_0^\tau \vec{G}_r(t) w(t) \cdot \vec{r}(t) dt \tag{2.10}$$

where

$$w(t) = \begin{cases} 1 & 0 < t < \tau \\ 0 & \text{otherwise} \end{cases}$$

Applying the inverse Fourier transform to the gradient function, equation 2.10 takes the form

$$\varphi(\tau) = \gamma \int_0^\tau \left[\int_{-\infty}^{+\infty} \vec{\Gamma}_r(f) e^{j2\pi ft} df w(t) \right] \cdot \vec{r}(t) dt \tag{2.11}$$

which can be reformulated as

$$\varphi(\tau) = \gamma \int_{-\infty}^{+\infty} \Gamma_r(f) \cdot \left[\int_0^\tau w(t) r(t) e^{j2\pi ft} dt \right] df \tag{2.12}$$

and simplified in

$$\varphi(\tau) = \gamma \int_{-\infty}^{+\infty} \Gamma_r(f) \cdot \left[W(-f) \otimes \vec{R}(-f) \right] df \tag{2.13}$$

A gradient function generalization based on the Fourier transform is defined by equation 2.13. In general, this function can be considered as a "filter" that measures the components of movement selectively. Assuming that $r(t)$ operates as a representation of a simple linear motion, its complex motion is given by

$$r(t) = r_0 + \vec{\xi}(r,t) \tag{2.14}$$

where $\vec{\xi}(r,t)$ is the displacement of the spin from its average position. In the specific case of a harmonic propagation wave, the position vector can be a pure sinusoid and therefore be expressed as

$$\vec{r}(t) = \vec{r_0} + \vec{\xi_0} e^{j(\vec{k}\cdot\vec{r} - \omega t + \theta)} \tag{2.15}$$

where ω is the angular frequancy of the mechanical armonic excitation, θ is the initial phase offset, k is the wave number, and $\vec{\xi_0}$ is the peak amplitude of the spin displacement from its average position. Under these conditions, it is useful to consider a basic function $\vec{G}_r(t)$ that is switched in polarity at the same frequency as the position vector, whose amplitude results to be

$$|\vec{G}_r(t)| = \begin{cases} +|G| & \in [nT, (2n+1)T/2) \\ -|G| & ((2n+1)T/2), (n+1)T] \end{cases} \tag{2.16}$$

where n=0,1,2,...,N-1, $T = 2\pi/\omega$ is the gradient force. If the time period τ is chosen so that $\int_0^\tau G_r(t)dt = 0$, the observed phase shift in the received signal is given by

$$\varphi(\tau, \vec{r}) = \gamma \int_0^{\tau = NT < TE} \vec{G}_r(t) \cdot \vec{\xi_0} e^{j(\vec{k}\cdot\vec{r} - \omega t + \theta)} dt \tag{2.17}$$

which results in

$$\varphi(\tau, \vec{r}) = \frac{2\gamma NT(\vec{G}\cdot\xi_0)}{\pi} \sin(\vec{k}\cdot\vec{r} + \theta) \tag{2.18}$$

where N is the number of gradient cycles, T is the period of mechanical excitation and TE is the echo time of the MR signal. Equation 2.18 shows

that the measured phase transfer is related to the scalar product of the displacement vector and gradient vector and the period and number of gradient cycles. This latter dependence causes high sensitivity to small cyclic amplitude shifts associated with acoustic wave propagation, constantly accumulating phase changes over several cycles of mechanical excitation and gradient waveform. This equation also indicates that the measured phase shift also depends on the initial phase offset between the gradient waveform and mechanical excitation. In addition, if a sinusoidal gradient is chosen, the gradient waveform is given by

$$\vec{G}_r(t) = \begin{cases} \vec{G}_0 \cos(\omega t) & t \in [0, nT] \\ 0 & \text{otherwise} \end{cases}$$

and applying the same analysis made for the equation 2.15 and 2.17, the phase shift results to be

$$\varphi(\tau, \vec{r}) = \frac{\gamma N T (\vec{G} \cdot \vec{\xi}_0)}{2} \cos(\vec{k} \cdot \vec{r} + \theta) \tag{2.19}$$

This equation suggests that displacements occurring along any direction can be measured by changing the direction of the applied gradients. Two measurements with alternating gradient polarities are then acquired to reduce systematic phase errors are and increase sensitivity to small displacements. This balanced acquisition system reduces systematic phase errors and doubles the sensitivity to small displacements. The phase images of each acquisition are then subtracted to produce a difference image that reflects the phase shift caused by the mechanical propagation wave, and it is the reason for which such difference images are defined as *wave images*. Figure 2.12 shows both the waveforms (MEG) with opposite polarities used in sequence to produce the difference images and the time ratio between the MEG and the induced continuous sinusoidal motion [2]. The mechanical excitations are produced by a pneumatic system that incorporates an active driver (not MRI compatible) for the continuous production of acoustic waves, a passive driver (MRI compatible) positioned on the surface of the body, and a plastic tube in which air passes through to transmit the excitations from the active to the passive driver. Generally the active driver consists of a signal generator connected to an audio amplifier and a loudspeaker while the passive driver, for many abdominal applications, has a drum or disk design to maximize contact with the surface, and this can be applied to the body in any orientation (Figure 2.13).

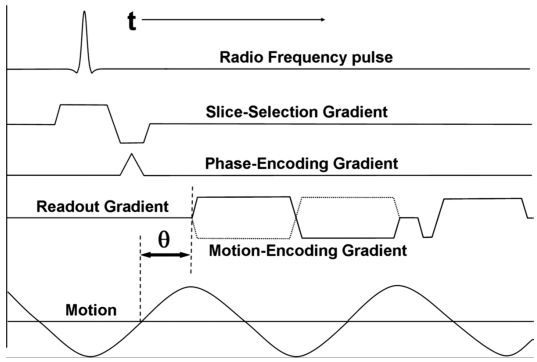

Figure 2.12: Example of a gradient-recalled echo MRE pulse sequence diagram [2]

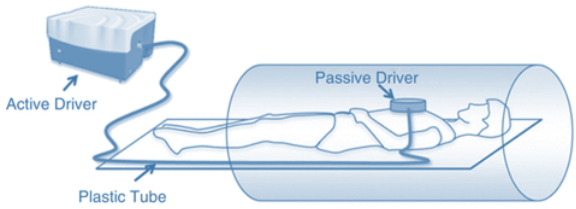

Figure 2.13: Pneumatic System MRE

The mechanical quantities that need to be characterized are those that connect the force to the deformation (stress-strain), and since the dispersions are very small in MRE (order of the microns), a linear relationship between them can be assumed. If the material is supposed to be isotropic, the problem is reduced to calculating two quantities independent defined Lamé constants λ and μ hich represent the longitudinal and shear deformation respectively. The isotropic relationship between stress and deformation is given by

$$\sigma_{ij} = 2\mu e_{ij} + \lambda \delta_{ij} e_{nm} \tag{2.20}$$

where e it is a component of the stress tensor and δ is the Kronecker delta. The stress tensor e_{ij} is defined in terms of displacement tensor u_{ij} as

$$e_{ij} = \frac{u_{ij} + u_{ji}}{2} \tag{2.21}$$

Replacing this quantity in equation 2.20, gives the general equation for har-

monic movement in an isotropic and linear elastic medium

$$[\lambda u_{ji}]_i + [\mu(\frac{u_{ij} + u_{ji}}{2})]_j = -\rho\omega^2 u_i \tag{2.22}$$

where ρ is the density of the material and ω is the angular frequency of the mechanical oscillation. To simplify the wave equation, local homogeneity is assumed, so that λ and μ are not position functions and equation 2.22 becomes an algebraic matrix equation that can be solved locally by direct inversion, that is

$$\mu\nabla^2\mathbf{u} + (\lambda + \mu)\nabla(\nabla \cdot \mathbf{u}) = -\rho\omega^2\mathbf{u} \tag{2.23}$$

where bold terms represent column vectors. In general, the longitudinal wavelength is very long in tissues (tens of meters) that the precise estimate of λ is very challenging, in addition, the longitudinal waves are much larger than shear waves. For these reasons, assuming that the displacements due to the longitudinal wave vary slowly and are therefore irrelevant, λ is eliminated from the analysis. Under this hypothesis equation 2.23 is simplified into a single vector equation

$$[\nabla(\nabla \cdot \mathbf{u}) + \nabla^2\mathbf{u}]\mu = -\rho\omega^2[\mathbf{u}] \tag{2.24}$$

Lameé constant μ is a complex quantity in which the imaginary part reflects the attenuation of a viscoelastic medium and for a harmonic motion is defined as

$$\mu = \mu_r + \mu_i = c + i\omega\eta \tag{2.25}$$

where c is the elastic stiffness and η is the material viscosity. Considering the case of propagation in an isotropic, homogeneous, incompressible medium without attenuation, a simple shear wave propagates with a specific spatial frequency f_{sp} and the shear modulus is

$$\mu = \rho\frac{f_{mech}^2}{f_{sp}^2} = \rho v_s^2 \tag{2.26}$$

where f_{mech} is the mechanical driving frequency and v_s is the wave speed. If there is attenuation the wave velocity and the attenuation depend on the frequency and are defined respectively as

$$v_s^2 = \frac{2(c^2 + \omega^2\eta^2)}{c + (c^2 + \omega^2\eta^2)^{\frac{1}{2}}} \tag{2.27}$$

and

$$\alpha^2 = \frac{\omega^2}{2} \frac{(c^2 + \omega^2\eta^2)^{\frac{1}{2}} - c)}{(c^2 + \omega^2\eta^2)} \tag{2.28}$$

The real "cutting module" is the real part, which describes the behavior of a static object in equilibrium. However, some processing techniques do not deal with attenuation but only calculate the local wavelength and estimate its velocity and then calculate an "effective" or "shear stiffness" modulus which is defined as the square of the wave velocity. These techniques are presented below.

Local Frequency Estimation (LFE)

First, the local spatial frequency of the shear wave propagation pattern is estimated using an algorithm that combines local estimates of instantaneous frequency on different scales. Through filters that are a product of radial and directional components and can be considered as lognormally oriented square waves these estimates are derived [17]. Assuming that $\rho \sim 1.0$ the shear stiffness is given by

$$\mu = \frac{f_{mech}^2}{f_{sp}^2} \tag{2.29}$$

It can be shown that, under the assumption of incompressibility, local homogeneity and without attenuation, this method solves the Helmholtz equation.This algorithm allows the estimation of μ from a single image using the displacement values for only one direction and one phase offset, but is also applicable to the case of complex harmonic displacement, obtained from several phase offsets. The limited resolution is a drawback, in particular the LFE estimate is inaccurate on sharp boundaries and the right one is only reached in a given area on half wavelength. Consider, for example, a rigid object with dimensions equal to a quarter of the spatial wavelength, embedded in a less rigid material. The LFE algorithm detects the rigid object but will never give a correct estimate of its shear stiffness.

Phase Gradient(PG)

After extracting the harmonic component at the drive frequency, both amplitude and phase (relative to an arbitrary zero point) characterizing the harmonic oscillation at each pixel of the image are obtained. If the movement is a simple shear wave, the gradient of this phase is exact the value

desired: the variation in phase per pixel, easily convertible to a local frequency and therefore to the shear rigidity. In general, this analysis can have a very high resolution, but it is very sensitive to noise and usually a gradient average is required. This technique produces inaccurate results when two or more waves are superimposed (for example, reflected waves) or when the movement is complex, since the phase values do not represent a single propagation wave.

Algebraic inversion of the differential equation(AIDE)

The Algebraic Inversion of Differential Equation (AIDE) indicates the direct inversion of the motion equations 2.23 and 2.24, with the hypothesis of local homogeneity. These equations can be solved separately at each pixel using only data from surrounding regions to estimate local derivatives. The algebraic inversion of the differential equation 2.23, evaluates the Lame coefficients for an isotropic material and needs all the components of motion [18]. Consider equation 2.23, which can be rewritten as

$$A \begin{bmatrix} \lambda + \mu \\ \mu \end{bmatrix} = -\rho\omega^2 \begin{bmatrix} u_1 \\ u_2 \\ u_3 \end{bmatrix} \tag{2.30}$$

where

$$A = \begin{bmatrix} A_{11} & A_{12} \\ A_{21} & A_{22} \\ A_{31} & A_{32} \end{bmatrix} = \begin{bmatrix} u_{i,i1} & u_{1,ii} \\ u_{i,i2} & u_{2,ii} \\ u_{i,i3} & u_{3,ii} \end{bmatrix} \tag{2.31}$$

The solution of 2.31 is given by

$$\begin{bmatrix} \lambda + \mu \\ \mu \end{bmatrix} = -\rho\omega^2 (AA^*)^{-1} A^* \begin{bmatrix} u_1 \\ u_2 \\ u_3 \end{bmatrix} \tag{2.32}$$

Assuming that the longitudinal pressure varies slowly, its derivative is negligible, and therefore in equation 2.32 the term λ can be omitted. Furthermore, considering an incompressible material, from equation 2.26 we have

$$\mu = -\rho\omega^2 \frac{u_i}{\nabla^2 u_i} \tag{2.33}$$

It should be noted that LFE and AIDE techniques correctly manage wave reflections and other complex interactions as they are based on the basic

motion equations, unlike the PG technique. The images of the mechanical properties calculated using MRE, result to be stiffness maps called elastograms, where the stiffness of the tissues is expressed in kiloPascal (kPa) and displayed in color scale. Figure 2.14 shows both the traditional abdomen

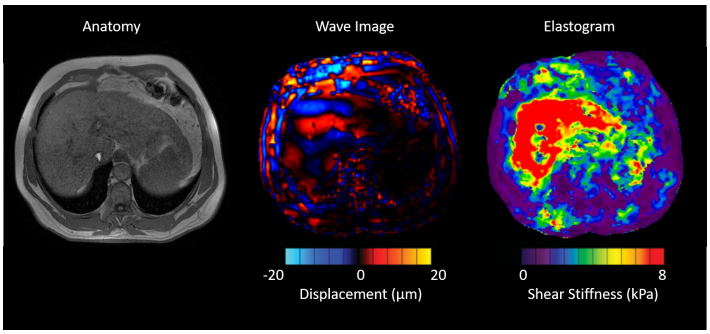

Figure 2.14: MRI and MRE images of the abdomen. From left to right: MR image, Wave image and Elastography image.

MRI image, the wave image obtained by MRE and the related color elastography map. From this map it can be observed that the stiffer regions assume higher values (kPa) than the soft regions that appear darker.

2.2.3 Applications

Liver

Cirrhosis of the liver is the end result of many types of liver diseases and is characterized by diffuse nodules and the formation of fibrous tissue that leads to a liver malfunction both from a metabolic and synthetic point of view. This organ, in fact, is the main gland of the body, located in the upper abdomen, on the right, under the diaphragm and performs many functions, including: production and storage of energy, creation of essential plasma proteins, filter and neutralization of toxic and pharmacological substances, supply of elements for blood clotting, as well as secretion of bile in the duodenum. Figure 2.15 shows the difference between scar tissue caused by cirrhosis and healthy liver tissue. In the past, as the only reference tool for the characterization of liver fibrosis, biopsy was used, an operation still in use during which a piece of liver is removed and examined. However, liver biopsies are invasive, usually inaccurate and make monitoring of the liver

over time difficult. Normally, healthy liver tissue is very elastic compared to diseased tissue, making elasticity a key property in the diagnosis of liver fibrosis. Magnetic resonance elastography imaging has been developed as an

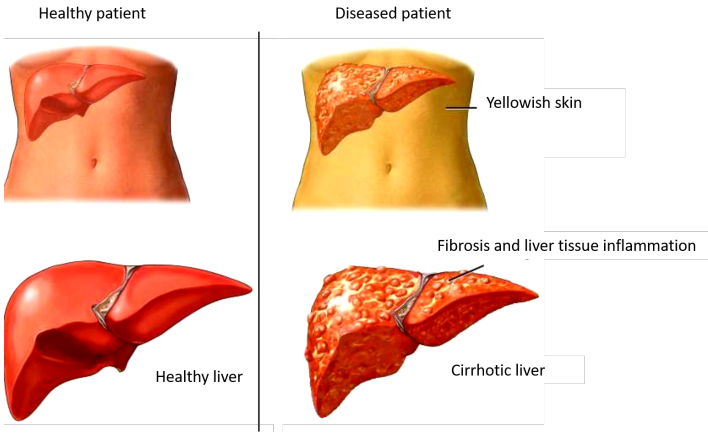

Figure 2.15: Tissue characteristics of normal and cirrothic liver.

alternative, reliable and non-invasive method for the detection and staging of hepatic fibrosis since it has been suggested that changes in the mechanical properties of the liver tissue, such as elasticity and stiffness, may correlate with this pathology. This medical exam is performed at a 60 Hz frequency using active pneumatic pressure drivers, acquiring wave data with four phase offsets and using a modified direct inversion rigidity estimation algorithm with multiscale functionality. The passive driver, in this case, is applied on the abdomen and held still by a patch elastic. The graph in Figure 2.16, based on [19], reports liver stiffness in some volunteers with healthy liver and in patients with liver in different stages of fibrosis. The graph is obtained by reporting on the abscissae the case of normal liver and the various stages of fibrosis, from F0 to F4, while on the ordinates the corresponding values of mean stiffness. As can be seen, liver rigidity is directly related to the various stages of the disease and increases as the disease progresses. Figure 2.17 shows the wave images and elastogram of four patients with hepatic fibrosis ranging from F1 to F4. It can be seen that both tissue stiffness and wavelength increases as the various stages of fibrosis progress. It has also been discovered that MRE can differentiate between malignant and benign liver tumors since the former have a greater average shear stiffness than the

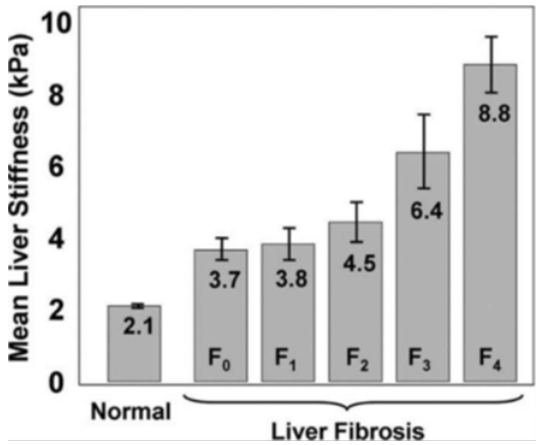

Figure 2.16: Liver stiffness values in both healthy and fibrosis patients.

latter and healthy tissue.

Brain

As already stated at the beginning of this chapter, palpation is the technique most widely used by a physician to arrive at a diagnosis. Doctors, in fact, using the sensitivity of the hands, and their detailed knowledge of the body, can assess the painful part of the body before the disease is identified. However, there is one organ that cannot be accessed except in the operating room: the brain, since this organ is protected both by the skull and the cerebrospinal fluid. Initial MRE studies of the brain were done on some slices of tissue and reported mechanical property values for global brain tissue, later, studies on the mechanical properties of both white and gray matter were performed. More recently, MRE has developed into a technique that can provide measurements of specific neuroanatomical regions such as corpus collosum, hippocampus, and corticospinal tract. In addition, healthy aging, gender differences, and a wide range of focal and diffuse brain diseases have been investigated. Quantitative measurements of the elastic modulus of brain tissue in addition to characterizing the related lesions are also used for biomechanical studies of brain trauma and in the development of neurosurgical simulation techniques. The frequency typically used during the elastographic examination of the brain varies from 10 to 100 Hertz. Waves

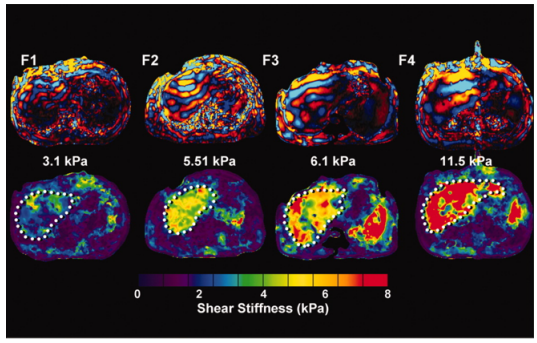

Figure 2.17: Liver stiffness values in four patients at various stage of fibrosis.

lower than 10 Hz allow the analysis of deeper brain tissue as they attenuate less quickly, however, are not used because they provide an unacceptable signal due to the too large wavelength. On the other hand, high frequency waves with a shorter wavelength can theoretically provide a higher spatial resolution but those above 100 Hz are generally not used due to discretization errors. In general, most of the MRE studies of the brain have been carried out using a frequency of 50-60 Hz which allowed an appropriate compromise between the penetration depth and the power and noise levels resolution. The pneumatic system, shown in Figure 2.18 is composed of an active driver that produces acoustic waves and is located in a different room from the one in which the MRI is performed, while the passive driver consists of an air pillow on which the back of the patient's head rests [3]. Figure 2.19 shows images of the brain of a patient with meningioma [4]. Specifically, the left image is a T1 MRI showing the position of the tumor, while the center and the right image represent the wave image and the related elastographic map respectively. The latter shows that the tumor is substantially stiffer than healthy tissue.

Breast

The breast is a glandular organ, present in both sexes but highly developed in females. Breast cancer is a disease due to the uncontrolled multiplication of some cells of the mammary gland, which become malignant. Among the symptoms that could indicate its presence are palpable nodules, suspected radiological lesions (not palpable), micro calcifications of dubious clinical

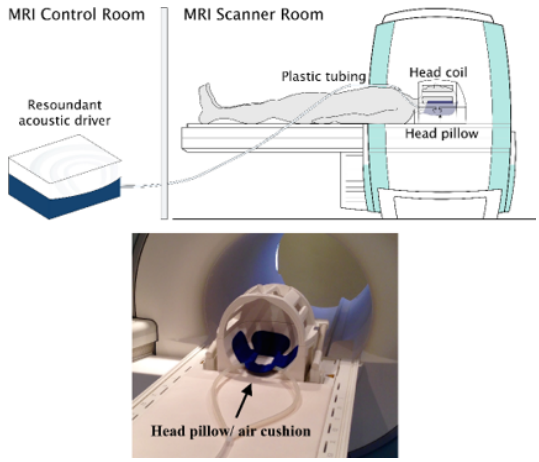

Figure 2.18: Schematic diagram of the pneumatic system used for the MRE exam of the brain [3].

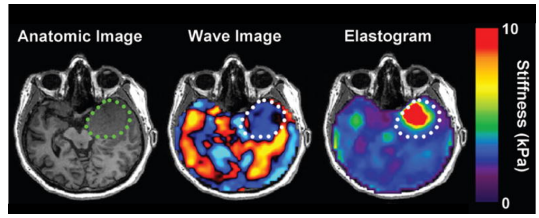

Figure 2.19: MRI and MRE images of brain affected by meningioma [4]

significance and blood secretions of the nipple. In Italy it is the most frequent tumor in women and affects one in nine women with an increased incidence, compared to the past, especially in the 35-55 years old population. Early diagnosis is important to treat the disease in its early stages, when the chances of recovery are higher. Although traditional imaging methods, such as mammography and MRI, contribute to the early detection of breast cancer, it has been found that they have significant limitations in detecting early changes in breast cancer and in distinguishing benign conditions from important pre-malign and malignant diseases. Compared to benign lesions, malignant tumors infiltrate the surrounding tissue leading to a pronounced reactive proliferation of connective tissue, which grasps greater tissue stiff-

ness, resulting in a reduction in tissue elasticity and homogeneity compared to benign lesions. Based on this, elastography magnetic resonance imaging has long been recognized as a method that offers considerable potential for discriminating malignant from benign tissues. To generate the acoustic shear waves, an electromechanical driver is used which is connected to two plates between which the breast is positioned. As can be seen from Figure 2.20, during the examination the patients are placed in an inclined position, with the breast positioned between two contact plates, which creates a minimum compression useful for stabilization. As an example of the effectiveness of

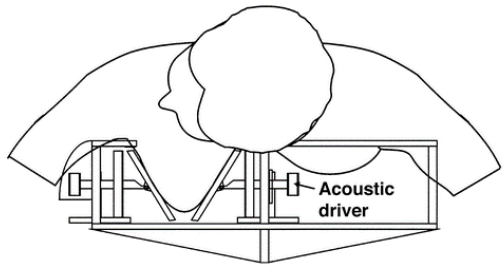

Figure 2.20: Device used for breast elastography, from [5].

this method, in distinguishing tumor tissue from healthy tissue, two cases of application are reported below, in vitro and in vivo [5]. In the first case an invasive carcinoma is diagnosed through the use of MRE in vitro, applied to a mastectomy performed on a 55-year-old woman. From Figure 2.21 (right)

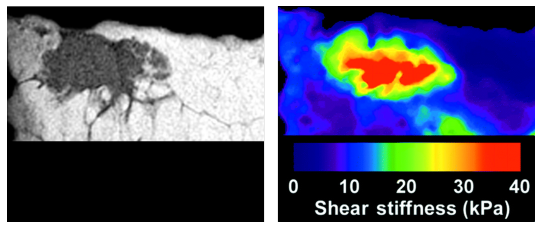

Figure 2.21: Surgical breast specimen. T1 MRI image is shown on the left and Elastogram map on the right, from [5].

it can be observed that the elastographic map shows highly stiff focal areas, corresponding to the tumor's location, delineating them from the softest tis-

sues around them. In the second case, images from the MRE examination of a breast cancer patient are shown. This examination was performed in vivo and from the elostagraphic map of Figure 2.22 a large area of high strength stiffness can be observed.

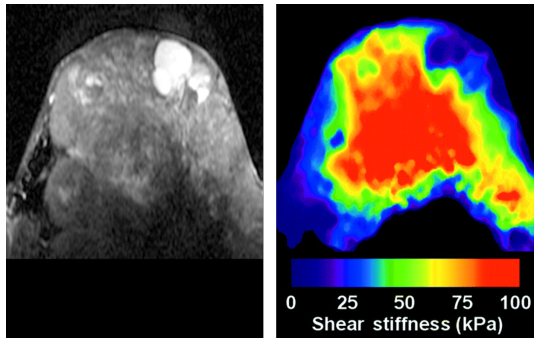

Figure 2.22: In vivo MRE on carcinoma patient. T2 MRI image is shown on the left and Elastogram map on the right, from [5].

Skeletal Muscle System

The musculoskeletal system is the set of bone, joint and muscle structures that support and defend the body and allow its movements. It is the most voluminous apparatus of the human body, of which it represents about 80 percent of the total weight. The human skeleton is a support structure placed inside the body, formed by a set of bones and cartilaginous tissue that supports the human body, and can be subdivided into in head , trunk and limb bones. The muscular system, on the other hand, is the set of tissues that allows the locomotion of the subject and the flow of internal organic substances such as blood and food. Usually the muscular system consists of two types of muscles, the voluntary or skeletal muscles, about 600, which are striped and allow the movement of the subject, and the involuntary muscles, also called visceral, due to their location, which are smooth and are found in the structures of the digestive tract, muscle tunics, and the muscle structures of blood vessels, especially in the arteries to allow the transformation of the pulsating flow of the heart into continuous flow. The MRE examination applied to this apparatus has the purpose of studying the rigidity of the skeletal muscle, which changes in relation to its contraction;

a possible increase in rigidity therefore means that the muscle is sick or damaged. Figure 2.23 shows an example of MRE examination on healthy patient in which images of the calf solus muscle are acquired; the MRI image of the muscle is shown and the green arrow indicates the position where the electromechanical driver used to create the shear waves has been placed (Figure 2.23 a). The examination was performed at 100 Hz frequencies and wave images were acquired while the muscle exerted forces of 0, 5 and 10 N/m by means a leg press (Figure 2.23 b-d) [2].

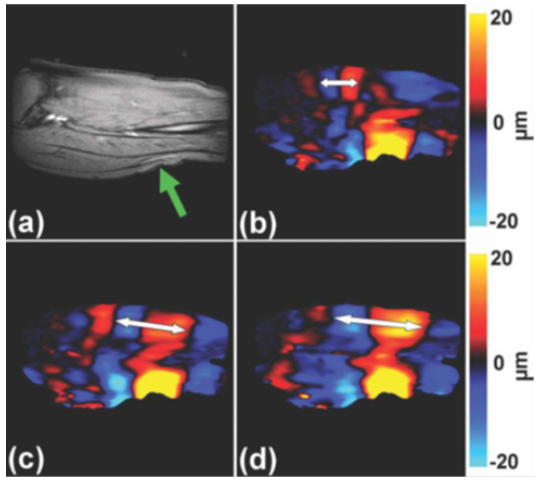

Figure 2.23: Skeletal muscle system wave images, from [2].

Chapter 3

3D medical imaging

In this chapter the use of three-dimensional anatomical models and 3D printing technology in the biomedical field will be discussed. An overview on the use of both virtual and physical simulators will be given evaluating their differences and advantages. In addition, it will be presented a simulation project developed during this thesis for preoperative planning in neurosurgery. Finally, four case studies, that have concerned the realization of a preoperative planning physical simulators for neurosurgical interventions of meningioma resection, will be presented.

3.1 3D model reconstruction

To date, the standard procedure for making a diagnosis and/or planning of surgery is based on the analysis of two-dimensional medical images. The acquisition devices based on tomography, such as CT and MRI, generate image sequences that allow a layered view of the investigated organ; each image represents a body section that is called a "slice". Nowadays these sequences are generated through increasingly innovative devices that allow the acquisition of a large area of the body in a short time obtaining high quality images. Such sequences can contain a very high number of images, sometimes even more than three hundred sections of the same organ are acquired. This means that the doctor will have to analyze a high number of slices in order to make a diagnosis, screening or surgical planning. These analyses are made on 2D images by evaluating the spatial positions of organs and malformations or benign and malignant neoformations in relation to the

surrounding tissues. Mentally reconstructing the analyzed anatomy in 3D and/or integrating information obtained through various acquisition devices is very complicated and sometimes not feasible. For this reason, anatomical models 3D reconstruction helps the physician to have a more complete and precise view of the anatomical region under examination. In this context, modern advances in 3D technology have enabled the development of anatomical models that provide a realistic representation of complex anatomies that can be used as an aid to diagnosis, surgical planning and training. In addition, the simplicity of these models also allows better communication with families. More specifically, reverse engineering, CAD (computer aided design) modeling, and AM technologies [20] enable the fabrication of patient specific and high-resolution 3D anatomical model, which provide a realistic and immersive training environment [21]. In the surgical simulation, an in-depth study of the clinical case through the customized simulator allows surgeons to reduce surgery times and complication rates by helping them to predict surgical crucial points, identify adapted surgical strategies, and improve surgical outcomes [22, 23]. The improvement of computer capabilities and the availability of more cost-effective medical image processing software and of affordable 3D printers could empower clinicians with more flexibility to design and execute personalized therapeutic plans. This enables satisfying the specific clinical needs of individual patients with affordable costs and reduced time, thus facilitating the mass personalization of the treatments, even during the daily practices of hospital departments. In particular, next generation 3D printers allow the perfect reproduction of internal anatomies that look, feel, and operate like real anatomies, without the need for further painting or assembly [24].

3.1.1 Virtual and physical 3D reconstruction

An accurate and a high-resolution 3D reconstruction of the patient's specific anatomy represents a major asset to the physician. The development of virtual (VS) and physical simulators (PS) has allowed us to overcome some limitations of the traditional methods using for diagnosis, training or preoperative planning. The virtual simulators, in addition to reproducing the specific anatomy of the patient, are also able to reproduce realistic environments necessary for an immersive simulation. Nevertheless, the vision of the anatomy on a flat 2D computer screen makes often interpretations related to depth difficult and the cost of the simulator is high. Quite the reverse,

physical simulators can be directly palpated, easily modified according to physician's request, incised by real surgical instruments and manipulated. Therefore, by using both physical and virtual simulators it is possible to overcome the limits of traditional medicine, allowing the physician to understand the spatial relationships between anatomical structures. In the surgical planning, the combination of virtual and physical simulation enables the identification of a set of promising surgical procedures that can be objectively compared to find the best intervention strategy. In addition, it allows to make easier and safer the necessary clinical practices for the treatment of patients, with the possibility of the clinicians to try procedures several times. Not by chance in the state of the art there are some works dealing with the combination of virtual and physical simulators into a single mixed reality system, linking benefits coming from having a physical scenario to interact with and the potentialities offered by virtual reality [25]. More specifically, the combination of VS and PS provide objective and repeated measurements to evaluate the performance, allows to easily change the anatomy offering residents the possibility to try the surgery not strictly on a single anatomy, allow the actual interaction with the simulated anatomy and permit to perform specific tasks with actual feedback. Among other things VS and PS, allow more precise and minimally invasive approaches reducing potential injury and eliminating the risks of serious complications and thus improving the experience and manual skills of the operator even in the management of possible situations of stress and error in crisis conditions.

3.2 Surgical simulators realization

In the next paragraph a method developed during this thesis work for the application of 3D technology on the realization of realistic surgical simulators for the treatment of brain tumors which integrate virtual and physical simulations will be proposed. In addition, four case studies concerning the realization of preoperative simulators used for the planning of neurosurgical interventions, will be presented.
Brain cancer surgery is a complex procedure that is not risk-free, and possible complications can arise and even cause irreversible neurological deficits for the patient [8]. The entire surgical procedure involves several phases: preoperative planning, preparation of the patient and the operation area, craniotomy, tumor resection, and skull and scalp closure, as shown in Figure

3.1. Preoperative planning can heavily influence the entire process, since

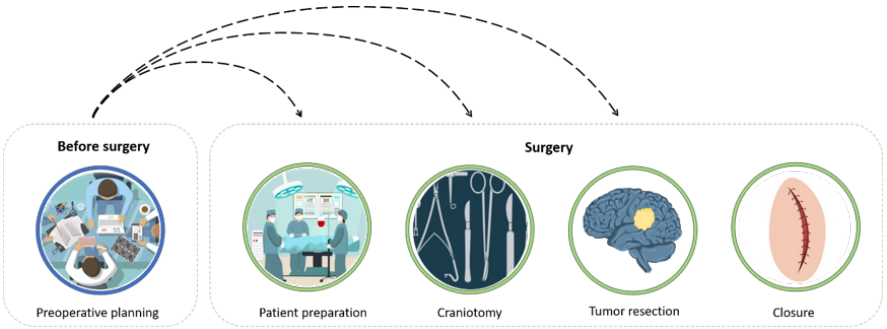

Figure 3.1: Brain surgery schematic pipeline. Preoperative planning drives the entire procedure.

during the simulation, the neurosurgeons can decide on their entire surgical strategy, including how to position the patient, how to perform the craniotomy, and how to access to the tumor. For these reasons, the surgical planning is considered to be a critical step in many interventions [26]. Once the patient is taken to the operating room, after the anesthesia administration, his head is immobilized, and the operating area is drawn on the scalp (i.e., patient preparation). During the craniotomy phase, the surgeon creates an arched curl on the scalp overlying the lesion and the soft tissue is bent to expose the skull. A drill is then used to perform craniotomy, where a bone flap is removed and stored. Once the craniotomy is completed,the surgeon accesses the brain tumor according to the pre-planned trajectory. Often, the resection phase evolves entirely under an operating microscope [27] and partial or total brain cancer is removed. At the end of the procedure, during the closure phase, the removed bone flap is repositioned on the skull, is fixed with titanium plates and screws, then it is sutured.
Before surgery, the time the surgeons devote a preoperative plan is essential and often determines the level of confidence they have during the intervention. During this step, the surgeon defines the surgical problem, first to fully identify all the anatomical and technical aspects of the procedure, and then to plan the approach. The first aim of the planning is to establish a correct diagnosis that starts from the visualization of multimodal data obtained from various imaging modalities. Such imaging modalities can be functional or structural such as magnetic resonance imaging, computed to-

mography, functional magnetic resonance imaging [28], and so on. Based on this information, the surgeon, that has a thorough knowledge of the relevant operative procedures and the related hazards and success rates, makes his decisions on how to manage the intervention [29, 30]. Preoperative planning is traditionally based on the identification of relevant anatomical reference points on tomographic data, on the measurement of the distance and angles between them, on the calculation of anatomical areas and volumes, and on the sketch of the possible trajectories for obtaining access to the tumor site. This process helps the surgeon to develop a correct 3D image of the problem in order to get a proprioceptive feel for the dynamics and complexity of the intervention to perform. Information on a surgical plan will ensure that the operating room staff has time to prepare for their patient and to identify and remedy potential difficulties [27]. The surgeon's experience is paramount for achieving adequate outcomes. Notably, to avoid violating functional areas, and even after careful preoperative planning, the surgeon could prefer to perform a conservative surgery rather than an effective resection of the tumor. Such a limitation can be overcome by providing the surgeon with a tool that is able to (1) accurately and objectively predict the risk of a complete tumor resection (2) provide a hands on experience of the surgery.
The simulation process developed in this work consists of the following phases (see Figure 3.2):

1. 3D reconstruction of the patient's anatomy
2. Surgery virtual planning
3. Fabrication of the bio-model
4. Surgery simulation (the surgeon uses a hands-on bio-model to simulate the surgery)

In the following paragraphs, the various phases of the simulation process are described in detail.

3.2.1 3D Reconstruction

The complete simulator manufacturing process includes some key steps represented in Figure 3.2 that, starting from 3D reconstruction of the patient anatomy, leads to the creation of 3D anatomical physical replica. An effective simulator for preoperative planning and simulation requires an exact

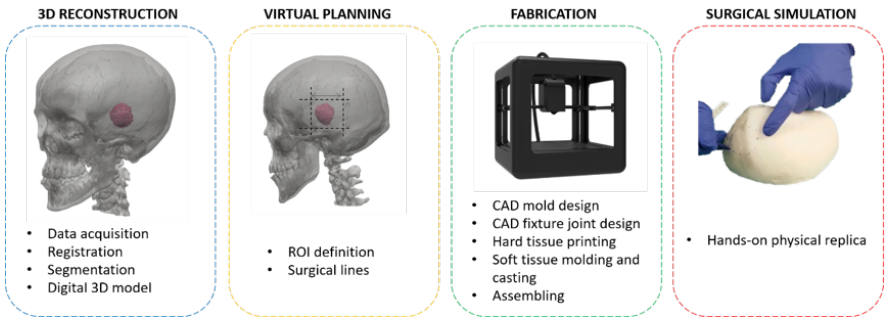

Figure 3.2: Simulation process pipeline.

patient specific geometry 3D reconstruction. The first step consists of the acquisition of patient medical images (i.e., CT/MRI) that provide anatomical information. More specifically, MRI better represents many soft tissues, thus enabling an accurate segmentation and 3D reconstruction of tissues such as the brain and blood vessels. Instead, the reconstruction of bones is performed from the segmentation of a CT scan, which provides a clear variation between calcium-based tissues and other types of tissues in gray values. Since information gained from different images acquired in the clinical track of events is usually of a complementary nature, a proper integration is often needed. The first step of the integration process is to find the spatial transformation that best aligns different datasets, a procedure referred to as registration [31]. Such registration can be performed both in the 2D domain and in the 3D domain (i.e., after the reconstruction). The former requires the manual or automatic identification of several significant anatomical landmarks on both the considered modalities (usually CT scan and MRI scan). These are elaborated upon by specific image processing algorithms (i.e., mutual-information based [32] or Deep Neural Network based [33] algorithms), to determine the spatial roto-translation transformation needed to move the reference dataset into the coordinate system of the target dataset [34]. Registration in the 3D domain consists of the reconstruction of 3D models of anatomical structures from medical imaging and of the subsequent identification of significant 3D landmarks (in both the reference 3D dataset and in the target 3D dataset) As a result, by means of specific 3D processing algorithms (e.g., Iterative Closest Point [35] or Global registration algorithm [36]), the same spatial roto-translation transformation as in the image domain approach can be

used [37]. The development of 3D models, for neurosurgical purposes, involves the image segmentation [38] [39], of both soft tissues (e.g., brain, tumor, etc.) and hard tissues (e.g., skull bones). Segmentation is the partitioning of an image into significant regions to distinguish objects or regions from everything else ("background") and therefore the segmented image results to be binary. The easiest way to identify a region of an image is to draw an area that defines the Region Of Interest (ROI) and to evaluate the gray values only within it; often, as a result of the segmentation procedure, the ROI corresponds to the anatomical region of interest. The most basic attribute to use to define regions is the gray level or brightness of the image, but other properties such as structure can also be used. Thresholding by intensity / brightness is a simple technique for images that contain solid objects on a different background of brightness but uniform. Each pixel is compared with the threshold: if its value is higher than the threshold, the pixel is considered "in foreground" and is set to white if it is lower or equal to the threshold is considered "background" and set to black. A good result of this process depends critically on the choice of an appropriate threshold. In the ideal case, the gray level histogram includes two distinct distributions, representing objects "in foreground" and "background", without overlapping. Figure 3.3 shows an example of segmentation. In this case, skull is the region of interest, which, as shown in the figure, is isolated from the surrounding anatomical elements assuming a green color. Registration and segmentation

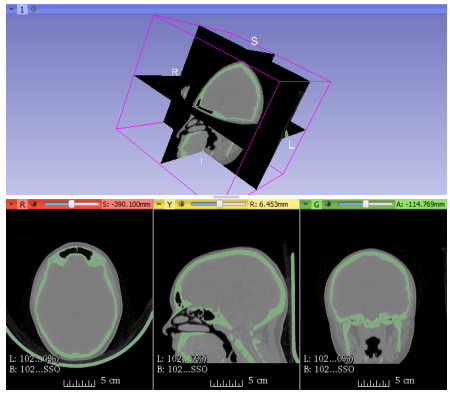

Figure 3.3: Example of skull segmentation using thresholding technique.

can be carried out with both commercial software (e.g., Mimics ®, Amira®,

etc.), and with open source software (e.g., 3D Slicer, OsiriX, ITK-SNAP, TurtleSeg, etc.). Within these software packages, once the segmentation of the anatomical element has been performed, the volume of the anatomical element is automatically obtained through embedded procedures, resulting in a three-dimensional configuration that can be stored in a 3D mesh file (i.e., an STL file format). An example of a digital 3D model is shown in figure 3.4. In order to focus the simulator on an optimized head replica, a region of interest can be first defined to specify the surgical interest 3D boundaries. Such an operation can be performed, using the surgeon's instructions in a commercial 3D modeling software environment (i.e., Fusion 360®, Geomagic Design XTM, Geomagic Freeform, Materialise 3-Matic, etc.,) or open source (i.e., Meshmixer, Blender). Such a process is needed to focus the simulation on a specific anatomical region, but could also be repeated to define the surgical lines needed to simulate the cranial resection process, thus leading the design to a partially operated simulator.

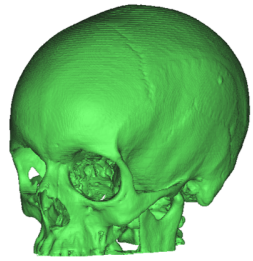

Figure 3.4: Example of a skull digital 3D model.

3.2.2 Virtual Planning

Once the 3D model is reconstructed, it is possible to perform a virtual planning of the surgical intervention. With reference to neurosurgery, the main aim is to virtually determine the best surgical approach needed to access to the region of interest (i.e., the area where the tumor is located). In other words, the surgeon has to decide the position and orientation of a series of cutting planes to remove the bone and to easily reach the intervention area. The virtual simulation is carried out thanks to minimal cooperation between the surgeon and the CAD engineer. In detail, by using an

information-sharing platform, the surgeon can autonomously manipulate 3D models and provide engineers with all the design constraints needed for the resection planes. In particular, the 3D modeler Forger®, a mobile-based polygonal modeler running with an iOS operative system, demonstrated its effectiveness in dealing with virtual surgical planning. With an intuitive touch screen interface, the surgeon can quickly pan, zoom, and rotate the 3D models and can easily add resection planes to the virtual model. Once the planes are correctly positioned on the model, it is possible to simulate the surgery by cutting the bone and soft tissues defined by the planes themselves (i.e., surrounding the tumor area). More different surgical strategies can be simulated using such a tool, to define the best approach (i.e., the minimally invasive one) to be further tested with the physical simulator. Moreover, the availability of the virtual model before and after the surgical simulation, allows us to manufacture the replica with and/or without the removed bone flap.

3.2.3 Fabrication

A rigid simulator part is certainly appropriate to reproduce the bone tissue but also, when needed, to reproduce a rigid replica of the soft tissues. The latter is preferred when neurosurgeon does not need to interact with the simulator through real surgical instruments, but instead needs to simply train the proprioception and observe the spatial relationships between the anatomical elements. When the simulation requires distinguishing soft tissues from rigid tissues, the soft parts are fabricated by casting silicon materials in rigid shell molds, thus following the same fabrication process of other rigid parts. Once the virtual simulation has been carried out and the region of interest has been defined, the physical replica can be manufactured. This phase is divided into two different steps: rigid part fabrication and soft tissues fabrication.

Rigid Parts Fabrication

The manufacturing process of rigid parts can effectively be performed with low cost 3D printer. Materials like Polylactic Acid (PLA) or Acrylonitrile Butadiene Styrene (ABS) [40] are commonly used as cost-effective materials to reproduce hard tissues like bones, thanks to their optimal properties such as model infill. Following negative feedback from some surgeons, wood-

loaded PLA (a material available on the market) was also tested to manufacture skull replicas. When PLA and ABS interact with the surgical drill, swarfs can be created adhering to the surface of the instrument, kneading it, and not allowing a correct and effective simulation of the cut. Wood-loaded PLA may represent a good choice to overcome this limit. In this case, the chip appears to be easily removable from the area of the tool, allowing us to easily perform the entire cutting procedure of the simulator. The separated structures need to be equipped by fixture joints to be assembled with accuracy after printing. CAD tools are employed to insert the anchoring systems between the various anatomical elements present in the ROI through the insertion of pins or other engineering/mechanical solutions. The 3D model of the parts prior to being printed, must be first processed and optimized by setting some printing parameters [41], which can be the same for each simulator sharing similar design requirements. The last step of the bio-model fabrication consists of the post-processing of the 3D printing output. When the prototype presents a poor surface finish, high porosity, the presence of appendices, supporting materials, and unfinished surfaces, an improvement can be obtained through a sandblasting process. The next step can involve the application of a resin coating to finish the surface of the final product. The resin is brushed on the object to fill all the model's cavities or indentations and to improve surface quality, thereby smoothing the roughness and reducing the stair stepping effect typical of a 3D printed object [42, 43].

Soft Tissues Fabrication

The low-cost soft tissues fabrication process combines 3D printing and some tissue-mimicking material casting. Soft tissue structures can be obtained by casting silicone rubbers in 3D printed molds. Indeed, the ultra-soft nature of some human tissues, such as the brain, can be replicated thanks to silicone rubber with different hardness ranging from the ultra-soft scale (shore 00 scale) to the soft scale (shore A scale). Other materials such as alginate, agarose, Polyvinyl Alcohol (PVA), Phytagel (PHY), Polyethylene Glycol (PEG), and polyurethanes are widely used in the literature [44], as their mechanical properties can mimic the elastic and haptic properties of human tissues. The fabrication process involves developing a mold design and engineering using CAD software. The mold is a negative replica of the anatomy, and it is fabricated with a 3D printing technique. The surfaces of release agents are then covered using an aerosol spray to prevent silicone

rubbers from sticking to the mold, impeding the removal of the physical replica from the mold. When the silicone is being mixed with the catalyst, colorants and silicone additives can be added to the mixture, in order to modify the chromatic and mechanical properties of the rubbers, such as the realism and the tactile performance of the final product. To improve the outcomes of the simulator fabrication process, a vacuum degassing system can be used to degas the mixture before pouring [45]. The mixture is then poured inside the mold and after the polymerization time,the silicone replica is removed from the mold. Ultra-soft silicone rubbers have sticky and oily characteristics, making them not easily manageable. For this reason, a post processing of the physical replica is needed, and it consists of sprinkling talcum powder on the replica, eliminating the sticky effect. The last step is to assemble the individual parts and may require the use of glues to keep the individual elements fixed.

3.3 Case Studies

During this thesis work, four case studies concerning the fabrication of preoperative simulators for neurosurgical interventions involving the resection of meningioma, were carried out. Written informed consent was obtained from the four patients, including for publication of both subjects' data and all accompanying images. All methods were carried out in accordance with the guidelines laid down in the Declaration of Helsinki.

3.3.1 Case 1

The first clinical case involved a sixteen-year-old girl suffering from a benign tumor at the base of the skull. The tumor was slightly compressing the optic nerve, thus making to accessing the tumor intracerebrally a hazardous process. The simulation objective was the identification of an alternative optimal surgical access option to preserve the optic nerve integrity. CT images (scanned with Philips Brilliance 64 machine; image size 512x512 px; xy spatial resolution 0.48 mm; slice spacing 0.40 mm) and T1 MRI images (taken with Philips Medical Systems; image size 512x512 px; xy spatial resolution 0.53 mm; slice spacing 1 mm) were acquired and saved in a DICOM (Digital Imaging and COmunications in Medicine) format. After obtaining the 3D reconstruction with Materialise Mimics, using first phase of the pipeline

shown in Figure 3.2, the STL file was imported into Geomagic Design X. (3D Systems, Inc., Rock Hill, SC, USA) to identify the region of interest together with the neurosurgeon's team. At a virtual level, several surgical lines were tested to arrive at the best strategy of intervention (Figure 3.5), which allowed us to preserve the primary brain areas and the optic nerve. Two fully rigid 3D models were manufactured with a 3D printer, one characterized by the entire anatomical portion involved in the intervention, the other instead faithful to the cuts identified at the virtual level. Both models were printed with MakerBot Replicator 2 (MakerBot, Brooklyn, NY, USA) with a PLA filament and are shown in Figure 3.5. In similar clinical cases, the pterional craniotomy is the traditional approach of accessing the tumor through the brain by opening the dura mater. Thanks to a careful preoperative planning, the neurosurgeon has been able to identify a transorbital route for the resection of the tumor that has provided for the removal of the bone of the orbit and the access to the tumor making the surgery minimally invasive and at low risk of brain damage.

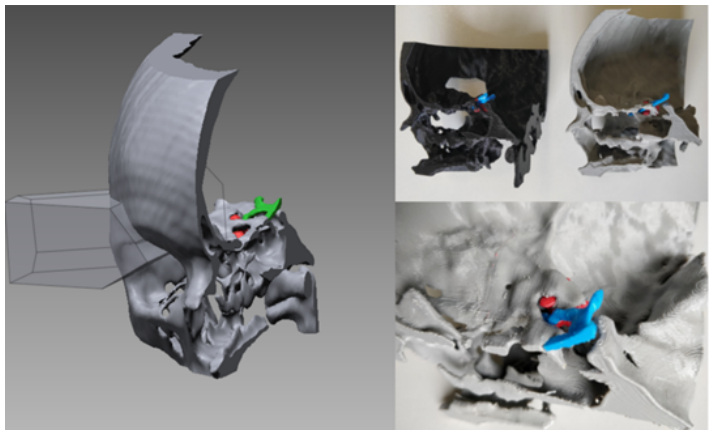

Figure 3.5: On the left, identification of cutting plans for access to the tumor; on the right biomodels fabricated in PLA. The black model was manufactured directly with the cut identified by the surgeon at the virtual level. The grey model reproduces the entire anatomical portion involved in the surgery.

3.3.2 Case 2

This case study focused on the fabrication of a simulator for the intervention of a 67 years old patient with a meningioma at the tentorium level. The position of the tumor required an accurate study of the geometry and spatial location of the meningioma placed near a venous sinus. The anatomical parts involved in the construction of the simulator were the skull, the tumor, the brain, the tentorium and the falx. CT images (scanned with Philips Brilliance 64 machine; image size 512x512 px; xy spatial resolution 0.48 mm; slice spacing 0.40 mm) and T1 MRI images (taken with Philips Healthcare/Ingenia; image size 256x256 px; xy spatial resolution 0.93 mm; slice spacing 1 mm) were acquired and saved in a DICOM format. Starting from the reconstructed digital 3D model obtained from CT segmentation with Materialise Mimics, the physician indicated the cut on the skull necessary to access the tumor area. Figure 3.6 shows the simulator that consisted of a replica of skull, brain and tumor; skull and tumor were manufactured directly in PLA, while brain was made in a super soft silicone rubber with a shore hardness of 00-50 (Ecoflex 00-50, Smooth-On, PA, USA) to replicate the mechanical characteristic of the actual human tissue. The manufacturing process of the soft tissue took longer than the direct 3D printing procedure of the skull and tumor. In fact, the negative of the brain was printed in Fused Deposition Modeling (FDM), a resin coating (XTC-3D, Smooth-On, PA, USA) was brushed on the surface of the mold to eliminate the stair stepping effect, after the cure time (4 h) the silicone rubber was poured into the mould to obtain the positive anatomical replica. Thanks to the use of simulators, it was possible to perform the operation in an optimised way, removing all the tumour tissue without affecting other anatomical areas.

3.3.3 Case 3

The third simulator involved planning the removal of a meningioma during the clinoid process in a 55 years old patient. The simulator aim was to increment the neurosurgeon awareness of the spatial relationships between the patient brain, the cancer and the big intracranial vessels. CT images (scanned with Siemens /Somaton Definition As+ machine; image size 512x512 px; xy spatial resolution 0.47 mm; slice spacing 1 mm) and T1 and T2 MRI images (taken with Siemens/Aera image size 256x256 px; xy spatial resolution 0.98 mm; slice spacing 1 mm) were saved in a DICOM format. In figure 3.7

Figure 3.6: Biomodel which consists in skull, brain and growth. Use of the neurosurgical microscope to observe the spatial relationships of the anatomical elements involved in the surgical procedure with the biomodel.

different views of the simulator are showed; it consisted in skull, brain and tumor. In particular, the skull and tumor were manufactured in FDM while for the brain the silicone Eco-flex 00-50 was used. At the digital level, the access cut to the tumor was identified so that the surgical route did not cross primary areas of the brain, thus reducing the risk of neuromotor and sensorineural deficits. The CT segmentation has been executed fully manually and supervised by the surgeon and radiologist, because of the low contrast of the tissue boundaries to be reconstructed.

3.3.4 Case 4

This case study concerns the manufacture of a simulator used in the case of a 76 years old patient with a meningioma located in the temporal lobe closely related to the meninges. The surgical operation consisted in separating the meninges from the tumor mass without affecting any tissue involved in the operation. CT images (scanned with Philips Brilliance 64 machine; image

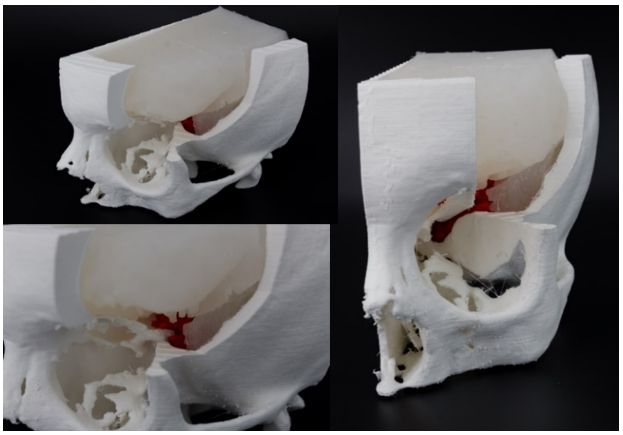

Figure 3.7: Different views of the biomodel that consist in skull, brain and tumor.

size 512x512 px; xy spatial resolution 0.48 mm; slice spacing 0.40 mm) and T1 MRI images (taken with Philips Healthcare/Ingenia; image size 512x512 px; xy spatial resolution 0.89 mm; slice spacing 1 mm) were acquired and saved in a DICOM format. In this case, the simulator consisted of four parts: skull printed in PLA loaded with wood fibre, brain and meningioma made with different silicones as tissues with different hardness (the first with Ecoflex 00-50 the second with Dragonskin 10), meninges reproduced with thin rubber sheet. In this case the cut was made physically on the simulator by the surgeon, using real surgical instruments. The simulator allows resident physicians to practice craniotomy centred on the lesion and therefore has primarily an educational purpose. The figure 3.8 shows the procedure that the surgeon performed on the physical model to simulate the entire surgery. In the first phase the possible access cuts were traced, the best cut was obtained by opening using the craniotomy drill, and after separating the layer of latex from the brain and tumor, the latter was removed.

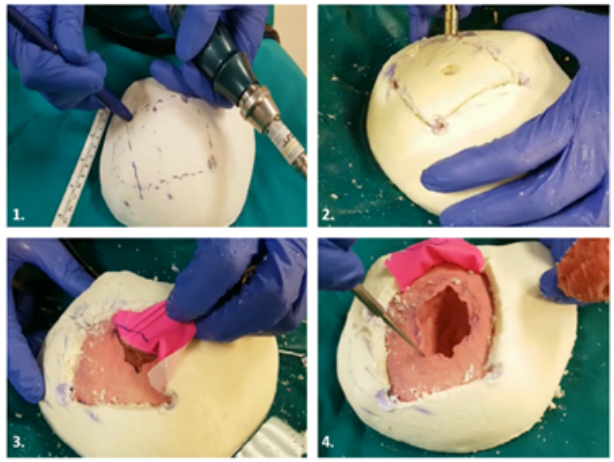

Figure 3.8: Simulation of the surgical procedure. 1. Skull flap tracking with surgical skin marker pens; 2. Craniotomy; 3. Separation of meninges from meningioma tumor; 4. Meningioma removal.

3.4 Concluding remarks

The introduction of 3D technology in medicine has completely changed clinical practice, allowing the exact reproduction of complex and geometrically difficult anatomical shapes with traditional production techniques. The development of simulators, virtual and physical, that faithfully replicate the specific anatomy of the patient, overcomes some limits of traditional methods used for diagnosis, training or preoperative planning. This leads to a better understanding of anatomical structures and the relationships between them, by the physician. In surgical planning, the combination of virtual and physical simulation allows to identify a set of promising surgical procedures that can be objectively compared to find the best intervention strategy. A deep knowledge of the patient's anatomical geometry is necessary to plan the best surgical strategy and to reduce the risk of surgical errors. In this context, it is clear how important it is to use surgical simulators that allow the doctor to simulate the operation before entering the operating room, improving self-confidence and reducing stress during the actual surgery. In particular, during this phase, the surgeon can test different surgical strategies in order to identify the best one in terms of results and time. During this thesis work,

a general pipeline was developed to produce a low-cost, patient-specific 3D anatomical model that allows surgeons to conduct a successful and accurate preoperative planning process. The pipeline is the result of a literature review of the use of 3D printing and tissue mimicking materials for surgical training and planning and aims to introduce neurosurgeons and clinical engineers to an internal, cost-effective preoperative simulation. The pipeline considers different manufacturing methods that can be used according to the challenge and goal of the preoperative planning, but that are also strictly dependent on the specific pathological case. Experience with the neurosurgery team of the Meyer Children's Hospital in Florence was reported, focusing on four 3D printed models that were used to plan surgeries according to the proposed pipeline. The simulators produced allowed the surgeon to identify, in some cases, alternative surgical pathways to traditional ones, thus avoiding the risk of neurological deficits caused by a possible injury of healthy tissue. In addition, better surgical results have been obtained thanks to an in-depth knowledge of diseased tissue volumes and spatial relationships with other anatomical regions. In conclusion, the methodology presented aims to provide a clear and systematic procedure to make the creation of physical simulators in clinical practice more accessible to provide benefits for both residents and senior surgeons involved in preoperative planning and simulation.

Chapter 4

Volumetric interpolation of biomedical images

In this chapter, volumetric image interpolation methods designed to increase the axial resolution of tomographic sequences and to obtain a refined 3D reconstruction are proposed and compared. The techniques considered are based on motion-compensated frame-interpolation concepts, which have been developed for video applications, mainly for frame-rate conversion. The performance of the proposed methods is quantitatively evaluated using sequences with a simulated low axial resolution obtained by decimation of standard high-resolution computed tomography sequences. Real low axial resolution data are also used for a qualitative evaluation of the proposed methods.

4.1 Introduction

As explained in the previous chapter, the 3D reconstruction of anatomical parts from medical images of the patient is a useful support to the physician in various clinical areas such as diagnosis, pre-operative planning, post-operative evaluation and teaching and training for medical students and junior doctors. An accurate "faithful to the original" shape of the 3D model enables to simulate a scenario similar to the real one, allowing to evaluate every possible aspect. For example, it allows to try different surgical strategies evaluating the difficulties that can be encountered and allows to investigate the possible solutions in advance, it also allows to verify the correct execution of the operation and to identify possible corrections. The

3D reconstructions are obtained by processing the image sequences acquired through different types of sensors. An accurate 3D reconstruction is possible if the processing procedure is performed on high axial resolution image sequences. On the other hand, very coarse reconstruction characterized by artifacts is obtained if the sequence consists of a few tomographic section. In this case we refer to low axial resolution sequence. This is the case, for example, of CT performed on neonatal patients suffering from craniosynostosis [46]. This pathology is a rare condition that affects one in 2500 live births and is characterized by an early suture of one or more cranial bone sutures, which leads to severe chronic endocranial hypertension and for which surgical correction is necessary.The CT scan has a high diagnostic accuracy and is the gold standard [47] to assess the severity of craniosynostosis although this acquisition may require sedation and presents risks due to the application of these particular rays, which have a specific absorption depending on the tissue or organ crossed, also subjects under 10 years of age are to be considered weak since they are particularly susceptible to malignant tumors caused by advanced radiation. The radiation dose is the amount of energy absorbed by the tissue per gram and its unit of measurement is Gray [Gy]. The unit of measurement of the Dose relative to the human body is called Dose Equivalent, and calculated as the Dose for a constant that takes into account the harmfulness of the radiation used. The enormous advantages of the CT make it extremely necessary in certain cases and make it possible to make a risk estimate that depends both on the application of the rays and the age of the subject. In the case of neonatal patient affected by craniosynostosis, due to the extreme importance of performing a CT scan, the application of X-rays is minimized and, compared to conventional scan, tomographic images can be obtained with a low dose or less ionizing radiation. As a result, the thickness of the CT sections is increased to compensate for the resulting loss of signal-to-noise ratio [48, 49] and, therefore, the axial resolution is reduced. Low resolution image sequences along the axial direction contain slices spaced by a significant step along the z axis and the voxel size is anisotropic. The application of this data for a 3D reconstruction produces models affected by the so-called *Lego* artifact [50]. In figure 4.1 are shown 3D models of the skull. In the left a 3D model reconstructed starting from an high resolution image sequence, in the right a 3D model affected by artifact due to the low axial resolution of the image sequence. A 3D model affected by artifacts cannot be used for pre-operative planning, training or diagnosis

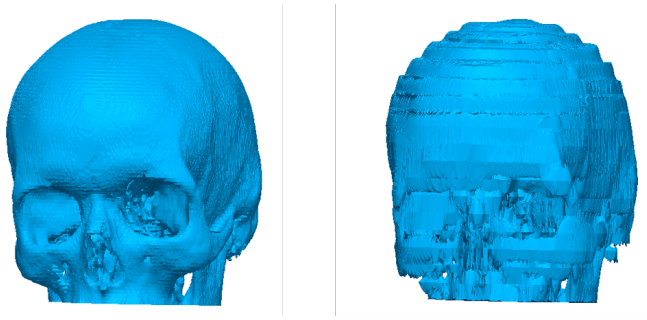

Figure 4.1: 3D model of skull reconstructed from a high axial resolution sequence (left) and a low axial resolution sequence (right).

as it presents an inaccurate anatomy that can lead the physician to incorrect evaluations. To solve this problem, interpolation between adjacent slices of the same sequence can be considered in order to increase the resolution in the axial direction and obtain volume data with isotropic dimensions. In literature, several axial interpolation methods, aiming at estimating one or more intermediate slices from two adjacent ones, have been proposed [51–53]. Image interpolation covers a wide range of techniques that can be classified as pixel-based [51–55] or object-based [56, 57]. In the first case, the pixels belonging to the input images are directly employed to estimate the values of the interpolated pixels, while in the second case, the interpolated image is constructed following a detection of the objects or features present in the input images. In this thesis work, the methods proposed focus on pixel-based techniques, which in the literature are often also referred to as registration-based methods and are proposed both in the case of 3D images and for the interpolation of four dimensional sequences, that is when the shape of the human anatomy changes during the acquisition time [58]. The problem of slice interpolation is similar to Motion Compensated Frame Interpolation (MCFI), which is a technique developed for several video processing applications, mainly in video rate encoding enables the generation of intermediate frames between those already existing. The purpose of this procedure is to make the animation more fluid by increasing the frame rate and reducing some artifacts such as motion blur and jerkiness [50, 56, 57, 59–61].

Figure 4.2 shows a scheme of the MCFI process that includes two main steps: motion estimationME and motion-compensated interpolation. The

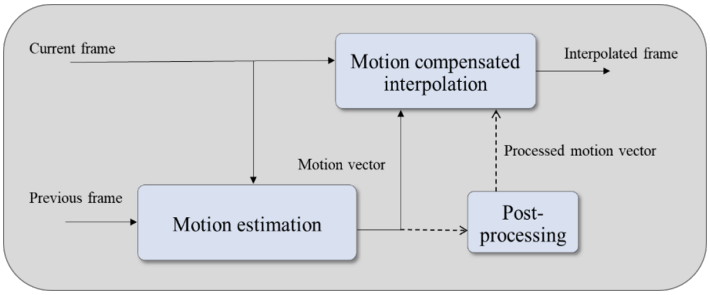

Figure 4.2: Scheme of motion compensated frame interpolation process.

goal of ME methods is estimating the motion vector field (MVF) between two consecutive frames. The most commonly used techniques of ME are Optical Flow (OF) [62], block-matching [63, 64] and phase correlation (in frequency-domain) [65, 66]. These methods calculate the MVF directly, i.e., by processing and comparing image pixels of subsequent frames. In order to reduce ME artifacts, post-processing of the estimated MVF may be applied. Furthermore, to avoid occlusions and to make the method more robust, the MVF can be calculated twice, in the forward and backward directions. The motion compensated interpolation operation allows the intermediate frame to be constructed by operating on the MVF obtained in the ME step [67]. The intermediate frame is generated by combining the current and past or future frames according to the estimated forward and backward MVFs. In this way, the two estimates complement each other in order to obtain a new interpolated frame of high quality.
In this thesis work, a method based on the OF algorithm is proposed. In the case of biomedical image sequences, even if the anatomical parts captured are not subject to a real movement in the adjacent slices, a spatial transformation (a sort of morphing) can be foreseen, able to relate the different slices to each other. For this reason, in the proposed method the MVF calculation is estimated using the optical flow technique, which is more suitable to describe smaller movements. In the next chapter all the steps of the proposed method will be presented in detail and different approaches are discussed depending on how the OF output is used, both pixel-wise and patch-based.

4.2 Displacement compensated interpolations

In this work, MCFI-inspired techniques are developed and applied to tomographic sequences with the aim of increasing the resolution of the sequences by means of an axial interpolation process. Figure 4.3 shows a schematic view of the proposed methods, whose steps will be detailed in the following subsections.

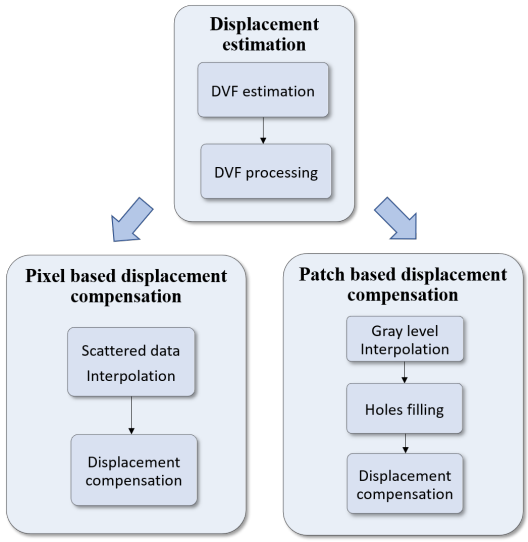

Figure 4.3: Block diagram of the proposed processing chain.

4.2.1 Displacement estimation

DVF estimation

A displacement estimation can be performed to calculate the displacement vector field (DVF) between two adjacent sections. Since the problem is analogous to MCFI, DVF is similar to MVF and the displacement estimation is computed employing algorithms taken from ME approaches. More specifically, in this study, an OF approach has been employed. Optical flow is a complete motion estimation method, because it calculates an independent motion for each pixel of the image by returning a dense field of motion vectors. The estimation is not performed directly on the real 3D motion of the

object under examination, but on the projection of the three-dimensional motion in a plane. Therefore the OF is an approximation of the 2D motion field (Figure 4.4). Given two consecutive images, if the motion vector field

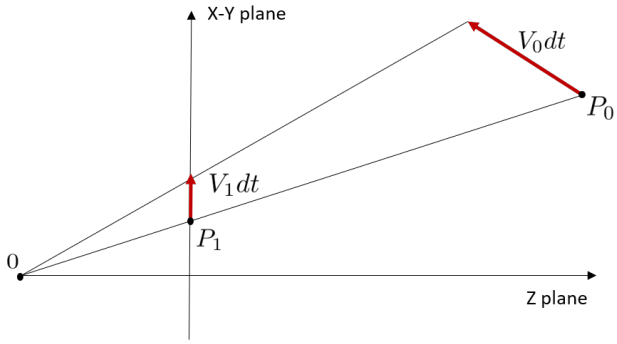

Figure 4.4: 3D motion projection on the image plane: $V_o dt$ vector indicates the real 3D motion vector of point P_0 and $V_1 dt$ indicates the motion vector projection on the 2D image plane.

is applied to each pixel of an image (reference image), it returns a prediction of the second image (target image).
The purpose of optical flow is to assign to each pixel belonging to the current frame a motion vector MV, which points to the position of the same pixel in a consecutive reference frame. It is known that to estimate the optical flow it is to consider that an object in motion, real or apparent, in an infinitesimal time Δt will move the amount Δx and Δy along the reference axes. If it is also considered the hypothesis that in this time interval the object's gray levels remain unaltered is obtained (uniformity)

$$I(x, y, t) = I(x + \Delta x, y + \Delta y, t + \Delta t) \tag{4.1}$$

Applying Taylor's serial development and the first derivative of the previous equation, which will result null for uniformity hypothesis, we obtain the optical flow constraint equation

$$I(x + \Delta x, y + \Delta y, t + \Delta t) = I(x, y, t) + \frac{dI}{dx}\Delta x + \frac{dI}{dy}\Delta y + \frac{dI}{dt}\Delta t + O \tag{4.2}$$

Assuming that the constraints of superior order (O) are negligible and

considering the hypothesis of uniformity it is obtained

$$\frac{dI}{dx}\Delta x + \frac{dI}{dy}\Delta y + \frac{dI}{dt}\Delta t = 0 \tag{4.3}$$

Calculating the derivative of I with respect to time, we obtain the equation of the optical flow constraint

$$\frac{dI}{dx}u + \frac{dI}{dy}v = -\frac{dI}{dt} \tag{4.4}$$

where $u = \frac{dx}{dt}$ and $v = \frac{dy}{dt}$.
The optical flow equation provides only the constraint along the gradient direction for the two components of the vector: for each pixel there is an equation and two unknowns.To solve this problem, several methods have been proposed in literature from which it is possible to obtain both a dense and sparse motion vector fields [62, 68–70]. In case of CT images, in order to obtain a correctly interpolated image, it is necessary to use an algorithm that allows a dense motion vector fields. This is possible, using, for example, the Horn & Schunck algorithm [62].This method introduces the constraint of motion uniformity in the neighboring pixels, at time t, which is defined by the following energy functional

$$E_{smooth}(f) = \iint_I [(\frac{du}{dx})^2 + (\frac{du}{dy})^2 + (\frac{dv}{dx})^2 + (\frac{dv}{dy})^2] dx\, dy \tag{4.5}$$

In addition to this constraint, it is also necessary to respect the optical flow constraint, which is defined in terms of energy

$$E_{data}(f) = \iint_I (\frac{dI}{dx}u + \frac{dI}{dy}v + \frac{dI}{dt}v)^2 dx\, dy \tag{4.6}$$

E_{data} is commonly called the data term and $E_{smooth}(f)$ smoothness term. Assembling the data term from 4.6 and smoothness term from 4.5 yields the total energy functional

$$E_{total}(f) = E_{data}(f) + \lambda E_{smooth}(f) \tag{4.7}$$

The parameter λ controls the smoothness of the estimated MVF and has a significant effect especially on areas with a low brightness gradient. The optimal value may depend on the type of processed images and is based on the energy of the error between the actual target image and the predicted

one. In the case of the CT imagery considered in this work, we found that $\lambda = \max \sqrt{E_x^2 + E_y^2}$, as suggested in [53], where E_x and E_y are the partial derivatives of the brightness of the image along x and y axes, actually gave the best performance.

DVF processing

It is known that MVFs are often affected by anomalies, for which different filtering methods have been proposed. The same is also true for DVF produced when OF algorithms are applied to CT sequences. In [71] , median filtering algorithms applied to vector fields have been proposed. These methods, also referred to as vector median filters (VMF), have the ability to suppress abnormal or outliers values, preserving their edges.The VMF has the task to regularize the obtained vectors grid, in fact assuming that the two compared frames can be affected by noise, it is necessary to reduce the influence of this, eliminating possible errors so as to obtain a more regular grid of vectors. In Figure 4.5 it is observed how the VMF goes to act in our case: the vector marked in red represents the displacement that has followed such pixel, this has opposite direction with respect to its adjacent ones, applying the filtering we obtain the right grid that results to be more regular.

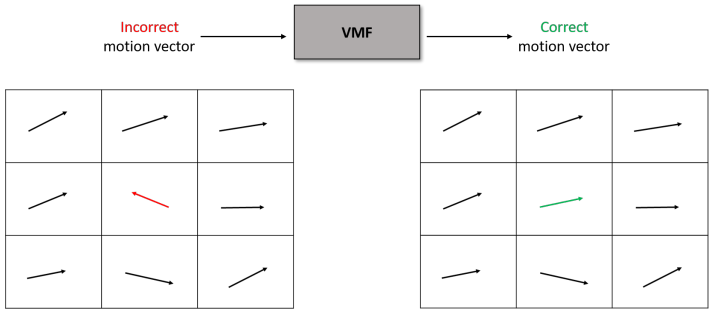

Figure 4.5: Example of vector median filters applied to motion vectors field.

Mathematically, given a set of N vectors $V = \{\mathbf{v}_1, \mathbf{v}_2, ..., \mathbf{v}_N\} \in R^N$, the vector-median is defined as the vector $\mathbf{v}_m \in V$ such that

$$\sum_{i=1}^{N} \|\mathbf{v}_m - \mathbf{v}_i\| \leq \sum_{i=1}^{N} \|\mathbf{v}_j - \mathbf{v}_i\|, \qquad j = 1, 2, \ldots, N \tag{4.8}$$

where $\|\cdot\|$ is the Euclidean norm. When VMF is applied to image filtering, the set V is composed by the motion vectors associated to pixels belonging to a (squared) neighborhood of the pixel to be filtered. A possible extension of the VMF, proposed in [72,73], consists in introducing a term that adjusts the filter selectivity by establishing a weight factor; this type of filter is called Weighted Vector Median Filters (WVMF). In this way, the points belonging to the window that are closer to the pixel concerned have more influence on the final result, while those that are further away are less decisive. Given the set of displacement vectors V and a set of weights $W = \{w_1, w_2, \ldots, w_N\}$, the weighted vector-median (WVM) of these values is the vector $\mathbf{v}_{\text{wvm}} \in V$ such that

$$\mathbf{v}_{\text{wvm}} = \arg\min_j \sum_{i=1}^{N} w_i \|\mathbf{v}_j - \mathbf{v}_i\| \qquad j = 1, 2, \ldots, N \tag{4.9}$$

In [72], the weights w_i are computed based on the energy of the error between the reference patch displaced by $\mathbf{v}_i$ and the target patch. More specifically, we have

$$w_i = \frac{D(\mathbf{v}_c)}{D(\mathbf{v}_i)} \tag{4.10}$$

where D is the energy of the displaced error and $\mathbf{v}_c$ is the displacement vector of the central pixel.

4.2.2 Pixel-based displacement compensation

Scattered data interpolation

DVF information is used to predict the displacement of objects and features from the reference slice to the target one. The reference image is denoted as $I_t(x, y)$, where t indicates a position along the axial direction, and (x, y) are the grid locations, which are assumed to be integer values. The prediction of the target image is denoted as $\hat{I}_{t+1}$. By using the DVF information and assuming a perfect prediction, we have

$$\hat{I}_{t+1}(x + v_x(x, y), y + v_y(x, y)) = I_t(x, y), \tag{4.11}$$

where $\mathbf{v}(x, y) = (v_x(x, y), v_y(x, y))$ is the displacement vector in the (x, y) position. The objective of slice interpolation is creating an intermediate slice, denoted as $\hat{I}_{t+\alpha}$. Reasoning in a similar way as before and assuming a linear

evolution along the axial direction, we have

$$\hat{I}_{t+\alpha}(x + \alpha v_x(x,y), y + \alpha v_y(x,y)) = I_t(x,y). \tag{4.12}$$

Since α and the components of $\mathbf{v}(x,y)$ are noninteger values, the interpolated image representation needs a resampling on an integer grid. Such a problem is also known as scattered data interpolation (SDI) and consists of constructing a bivariate function $F(x,y)$, which is as much smooth as possible and takes on a set of prescribed values $F(x_k, y_k) = f_k$, $k = 1, ..., N$, where (x_k, y_k) and f_k are known. The data are scattered in the sense that there are no hypotheses on their arrangement, apart from the fact that there are no repeated points. There are several methods for scattered data interpolation (SDI), each with its own peculiarities that make it particularly suitable in certain fields, depending on whether a global, local, computationally fast or extremely precise function is desired. The first two terms define the region of interest of the process; in fact *global*, as the name suggests, takes into account all the points of the surface while a *local* function considers small portions at a time, such as VMF. Finally, precision and speed of calculation are two inversely proportional characteristics since one tends to exclude the other, unless a compromise is found.

The principal SDI methods that can be found in the literature are: inverse distance weighting [74]; triangulated data [75]; radial basis functions [76].

In this study, we used the method based on triangulated data described in [77] and implemented into the Matlab function `scatteredInterpolant`. Interpolation methods belonging to this category operate through two preliminary steps:

- triangulation: it consists in connecting the sampled points in triangles.There are many types of triangulations with the aim of creating triangles with a shape as close as possible to that of the equilateral triangle. You have to choose the most appropriate one;
- localization: taking any point P inside the plane, you must find the triangle that contains it.

The most effective technique for this purpose is the Delaunay triangulation, named for the Russian mathematician. This triangulation is constructed in such a way that the circle circumscribing each triangle does not contain any other point in the scattered data set (Figure 4.6). These constraints, imposed on the circumferences, bring enormous advantages on the choice of triangles,

in fact they allow to maximize the least angle of these figures avoiding to obtain long and narrow figures (the optimal case is obtained for equilateral triangles). This procedure takes the name Max-in Angle Criterion [78].

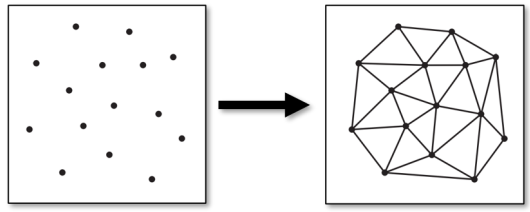

Figure 4.6: Example of Delaunay 2D triangulation, starting from a set of given points in the left.

Once a triangulation is obtained, the simplest interpolation that can be performed is the linear one by finding the plane through the three vertices. One of the main drawbacks of the methods based on the linear interpolation performed for each triangle is that, despite ensuring continuity of the solution within the figure, there is a discontinuity of the derivative along the edge, where there is contact between different triangles. Therefore we have that the function obtained is considered C^0 and not C^1. This characteristic requires to establish a relationship between the points belonging to the region considered and the external points, in order to avoid problems with the contour of the figure.

Forward and backward compensation

In a tomographic representation of anatomical parts, it may happen that the details of the organs are present only in one (both reference and target) of the adjacent slices. In this case it is not possible to reproduce intermediate versions of such details from an image that does not contain them. A similar problem occurs in video motion compensation when one object occludes another due to its relative motion. To partially solve this problem, it is possible to use forward and backward processing (where the reference and target images exchange roles). An example of forward and backward prediction is shown in figure 4.7. Let $\hat{I}^{(f)}_{t+\alpha}(x,y)$ be the interpolated frame obtained by using $I_t(x,y)$ and $I_{t+1}(x,y)$ as reference and target images, respectively, and let $\hat{I}^{(b)}_{t+\alpha}(x,y)$ be the interpolated frame obtained by using $I_{t+1}(x,y)$ and $I_t(x,y)$ as reference and target images, respectively (notice

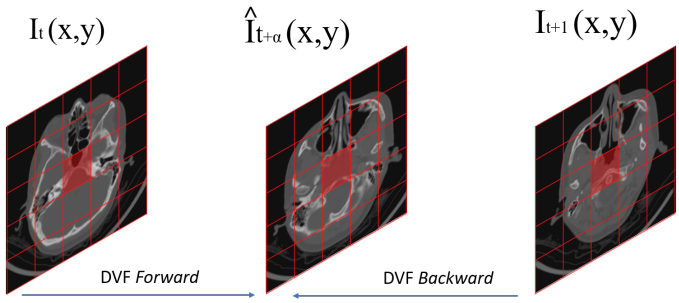

Figure 4.7: Forward and backward prediction.

that, in the backward estimation, α must be replaced by $1-\alpha$ in the l.h.s. of (4.12)). The final interpolated slice is then given by

$$\hat{I}_{t+\alpha}(x,y) = \frac{1}{2}\left[\hat{I}^{(f)}_{t+\alpha}(x,y) + \hat{I}^{(b)}_{t+\alpha}(x,y)\right]. \tag{4.13}$$

4.2.3 Patch-based displacement compensation

Patch-based interpolation

As explained in the 4.2.1 paragraph, applying a median filter after the motion estimation allows to eliminate possible anomalies and outliers. In addition to this processing step, a way to improve the regularity of the interpolated slice is to consider the image as divided into patches and work on each of them in a sequential way. This patch based approach, involves the calculation of the DVF as described in Section 4.2.1. The difference between this method and the pixel based one is the way the displacement compensation is applied. Considering a patch of a given size, the DV associated with each patch is the WVM of the set of DVs related to the pixels within the patch, so that, now, the whole patch undergoes the same DV. As in the case of scattered data interpolation, the DV is scaled by the α amount that depends on the position of the interpolated slice with respect to the adjacent ones. Also in this case, as in pixel based, the fact that both DC and α are not integer values, leads to a final spatial shift of the patch not integer. The situation is depicted in Fig. 4.8, where it is possible to notice that the pixels of the shifted patch are no longer on the whole grid, so it is necessary to find the values of the pixels of the missing slice (whose position is indicated with crosses) through

the interpolation of the surrounding ones. This problem, however, is much simpler than the scattered data interpolation described above. For example, the classic bilinear and bicubic interpolation can be used.

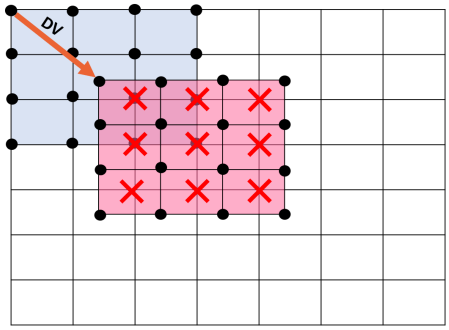

Figure 4.8: Interpolation scheme for the patch-based algorithm: shadowed rectangles represent the reference and the displaced patches; red crosses represent the interpolation grid positions.

Holes filling

In the patch-based method, patches within the frame of reference are selected so that they can be strongly overlapped. This has two advantages: first, overlapping patches produce multiple estimates of pixel values within the interpolated frame, which produces - averaging all values corresponding to the same position - a more accurate final estimate; second, the probability of having a pixel position without any estimate is reduced. As far as the latter problem is concerned, the presence of empty areas, i.e. in which no pixel has been associated, in the reconstructed slice is actually probable and, therefore, a "hole filling" algorithm must be provided. This algorithm proceeds in this way: first the holes are identified, then the values on the edges are interpolated linearly and the output is assigned to the pixels inside the hole. This procedure is repeated along both rows and columns, and then an averaging is performed. For example, with reference to 4.9 the algorithm fills the missing pixel of the first row of the hole region with the quantities

$$\hat{I}_{t+\alpha}(x,y+k) = \hat{I}_{t+\alpha}(x,y) + \frac{k}{3} \cdot [\hat{I}_{t+\alpha}(x,y+3) - \hat{I}_{t+\alpha}(x,y)], \quad k = 1,2 \quad (4.14)$$

and the missing pixel of the first column with the quantities

$$\begin{aligned}\hat{I}_{t+\alpha}(x-1+k,y+1) =& \hat{I}_{t+\alpha}(x-1,y+1) + \frac{k}{4}\cdot[\hat{I}_{t+\alpha}(x+3,y+1) \\ & - \hat{I}_{t+\alpha}(x-1,y+1)], \\ & k=1,2,3\end{aligned} \tag{4.15}$$

The Patch-based interpolation and holes filling procedures can be used both

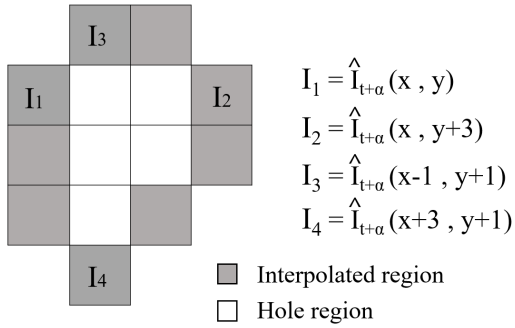

Figure 4.9: Holes filling algorithm.

in the forward and backward direction and the final missing slice is achieved by averaging the two estimates.

4.3 Experimental results

The process that leads to 3D model reconstruction from the input data, as discussed in Chapter 3, starts with a step of *segmentation*. The segmentation serves to identify, within each slide in the sequence, the pixels that belong to the organ/tissue that we would like to reconstruct. Each tissue - within the entire dataset - is identified by a certain range of gray values; for example, soft tissue is reproduced with low gray values while bone tissue is correlated to the highest gray values in CT scans. Segmentation [79, 80] can be performed manually, slice by slice, or automatically by selecting a gray level range for all slices. The 3D model of interest tissue is obtained by applying specific 3D voxel-based algorithms to the segmentation performed [81, 82]. If the slices axial interpolation considered in this work is applied, both the

image segmentation and consequently the final 3D reconstruction can be affected due to the introduction of any new intermediate gray levels in the estimated slices. For this reason, the performance of the proposed methods have been evaluated considering both the quality of the 2D interpolated images and the quality of the reconstructed 3D model. In both cases, objective indices were considered and a qualitative evaluation of the results obtained from the visual inspection was also compared with other interpolation algorithms taken from the literature.

4.3.1 Synthetically generated low-resolution sequences

High resolution sequences (HR) can be sub-sampled to synthetically generate low resolution sequences (LR). In this way, measurement indexes of the objective quality of the proposed method can be constructed by comparing the reconstructed slices with the original ones. More specifically, a complete CT scan is considered as the HR reference signal and a decimation along the axial direction produces the LR sequence. In this study, our HR data set is represented by two CT sequences, hereinafter referred to as CT1 and CT2, which reproduce the image of a skull and were acquired with a Philips-Brilliance 64 machine. The two sequences consist of 179 and 207 CT images, respectively, with a radiometric resolution of 12 bits. The slices have a spacing of 1 mm, a thickness of 2 mm and a size of 512x512 pixels; the downsampling factor was set to $M = 2, 3, 4, 5$. The performance of the proposed methods, developed in MATLAB environment, have been evaluated using the normalized 2D root-mean-square error (NRMSE) metrics, defined as

$$\mathrm{NRMSE} = \sqrt{\frac{\sum_{m,n}(x_{\mathrm{true}}[m,n] - x_{\mathrm{int}}[m,n])^2}{\sum_{m,n}(x_{\mathrm{true}}[m,n])^2}} \tag{4.16}$$

where x_{true} is the original image and x_{int} is the interpolated one. During the experimentation phase two algorithms were tested: one belonging to the pixel-based interpolation method (SDI), and one belonging to the patch-based method, described in the sections 4.2.2 and 4.2.3, respectively. In the latter case, linear and cubic interpolation within the patch grid have been tested: the two methods are indicated as PATCH-L and PATCH-C respectively. For PATCH-L a patch size of 5 was used (5 for PATCH-L and 7 for PATCH-C). All methods have used the WVM filter with which the displacement vector field has been regularized. The tables 4.1 and 4.2 show the results obtained in terms of average NRMSE on the slices just generated,

for the CT1 and CT2 sequences, respectively, using the SDI, PATCH-L and PATCH-C methods and varying the M decimation factor. In both are also reported the NRMSE values obtained with another method proposed in [53]; the latter high order slices interpolation method (here indicated as HOSI), is used to make a comparison. More specifically, HOSI was performed by setting the tolerance parameter (here indicated as tol) to values 0.04 and 0.001, resulting in a very different behavior in terms of performance and computational load

M	SDI	PATCH-L	PATCH-C	HOSI (tol = 0.04)	HOSI (tol = 0.001)
2	0.0604	0.0330	0.0315	0.0289	0.0245
3	0.0920	0.0642	0.0628	0.0648	0.0513
4	0.1166	0.0967	0.0952	0.1009	0.0779
5	0.1376	0.1281	0.1268	0.1303	0.1020

Table 4.1: Sequence CT1 – average NRMSE obtained by using different methods and varying the decimation factor.

M	SDI	PATCH-L	PATCH-C	HOSI (tol = 0.04)	HOSI (tol = 0.001)
2	0.0645	0.0366	0.0341	0.0347	0.0297
3	0.1110	0.0692	0.0672	0.0752	0.0606
4	0.1178	0.1027	0.9989	0.1096	0.0914
5	0.1390	0.1372	0.1361	0.1357	0.1165

Table 4.2: Sequence CT2 – average NRMSE obtained by using different methods and varying the decimation factor.

The performance of the proposed method has been evaluated both through a 2D analysis of the interpolated images and a study on 3D reconstructed models from the CT sequences, in which 3D metrics were used. The 3D reconstructions obtained from the original HR sequences are considered the reference model against which the approximate 3D model is compared, obtained from the axially interpolated LR sequence. For the reconstruction of the 3D models, MIMICS, a certified medical software, produced by Materialise, has been used, which allows to obtain 3D models after a process of segmentation of the anatomical parts of interest and eventually of further

elaboration processes. In Figures 4.10, examples of results of the segmentation process are shown; in particular, the skull detected by some original slices of the CT1 sequence is shown and compared with those obtained with the PATCH-C, HOSI (tol = 0.04) and HOSI (tol = 0.001) methods. Figures 4.11 show both the 3D models reconstructed from the interpolated sequence and those obtained from low resolution sequences (i.e. without applying any axial interpolation method).

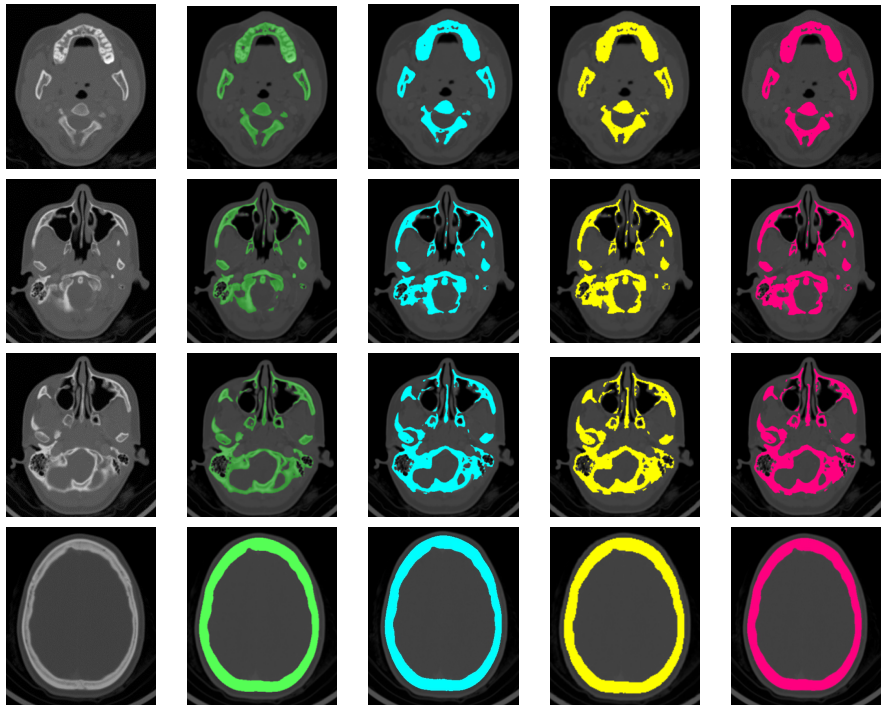

Figure 4.10: Accuracy of segmentation. First column: original grayscale sections; second column: segmentation maps obtained from original sections; third, fourth and fifth columns: segmentation obtained from interpolated sections ($M = 3$) by using PATCH-C, HOSI with tol = 0.04 and HOSI with tol = 0.001, respectively.

To compare two 3D reconstructions, two specific metrics were considered: the average value μ and the standard deviation σ of the distance between the reference mesh ("true") and the approximate one. These measurements

are obtained with Geomagic Design X software, a 3D Systems product. The tables 4.3,4.4,4.5,4.6 show the 3D metrics obtained from the methods under test and vary the M decimation factor. To appreciate the gain obtained by interpolation, the metrics calculated on the 3D model obtained using the LR sequence, that is without any axial interpolation (here indicated as "Raw"), are also shown.

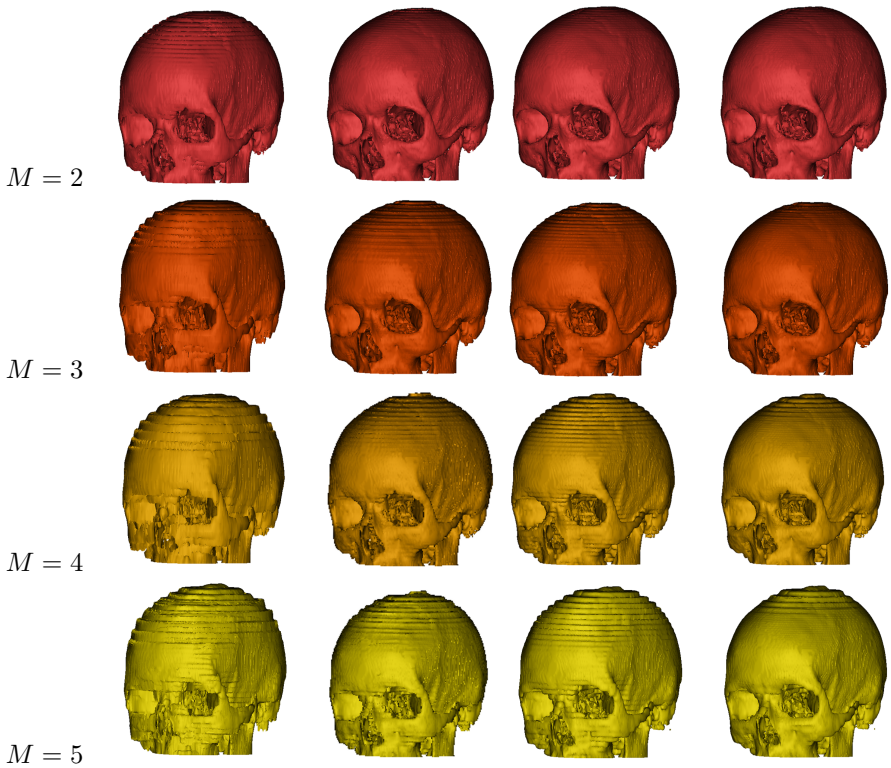

Figure 4.11: 3D models obtained from the interpolated sequences and varying with the decimation factor M: in the first column, the models obtained from the subsampled sequences; from the second to the fourth columns, the results obtained with the PATCH-C, HOSI with tol=0.04, and HOSI with tol=0.001 methods, in that order.

M	Raw		SDI		PATCH-L	
	μ	σ	μ	σ	μ	σ
2	0.290	0.470	0.007	0.108	0.007	0.112
3	0.869	0.908	0.315	0.394	0.221	0.360
4	0.960	1.208	0.451	0.573	0.294	0.504
5	1.020	1.233	0.743	0.789	0.521	0.706

Table 4.3: Sequence CT1 – average distance and standard deviations (in mm) between the 3D models constructed by using SDI and PATCH-L methods.

M	PATCH-C		HOSI (tol=0.04)		HOSI (tol=0.001)	
	μ	σ	μ	σ	μ	σ
2	0.003	0.062	0.007	0.144	0.001	0.025
3	0.217	0.362	0.250	0.417	0.152	0.329
4	0.290	0.504	0.439	0.645	0.275	0.524
5	0.519	0.717	0.731	0.879	0.460	0.717

Table 4.4: Sequence CT1 – average distance and standard deviations (in mm) between the 3D models constructed by using Patch-C method and the reference one.

M	Raw		SDI		PATCH-L	
	μ	σ	μ	σ	μ	σ
2	0.313	0.003	0.066	0.108	0.003	0.060
3	0.742	1.066	0.406	0.581	0.206	0.385
4	1.096	1.506	0.484	0.657	0.299	0.531
5	1.498	1.933	0.800	0.906	0.682	0.944

Table 4.5: Sequence CT2 – average distance and standard deviations (in mm) between the 3D models constructed by using SDI and PATCH-L methods.

M	PATCH-C		HOSI (tol=0.04)		HOSI (tol=0.001)	
	μ	σ	μ	σ	μ	σ
2	0.001	0.040	0.002	0.039	0.001	0.036
3	0.206	0.370	0.236	0.382	0.160	0.350
4	0.289	0.510	0.413	0.592	0.295	0.539
5	0.671	0.934	0.694	0.839	0.500	0.775

Table 4.6: Sequence CT2 – average distance and standard deviations (in mm) between the 3D models constructed by using Patch-C method and the reference one.

4.3.2 Real low-resolution CT sequence

In the case of real CT sequences with low axial resolution, as in the case of neonatal patients discussed in the introduction, it is possible to apply the proposed methods to obtain an accurate 3D reconstruction with limited artifacts (Lego effect). In Fig. 4.12, three examples of 3D models created from real low resolution CT sequences of neonatal skulls are shown. The first sequence (see results in the first row of Fig. 4.12) was composed of 82 slices, whereas the last two sequences (see results in the second and third row of Fig. 4.12) were composed of 41 slices. The results were obtained with an interpolation factor $M = 4$ and by using the PATCH-C, HOSI with tol=0.04, and HOSI with tol=0.001 methods.

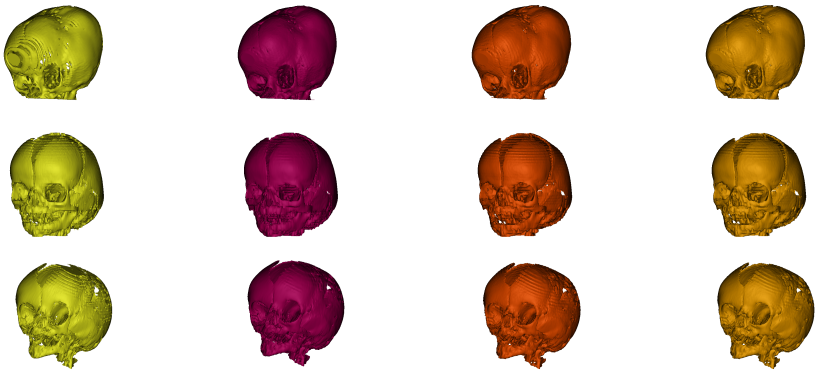

Figure 4.12: Examples of 3D reconstructions of skulls of neonatal patients: in the first column the models obtained from the original low resolution sequences; from the second to the fourth column, the models obtained by using the PATCH-C, HOSI with tol=0.04, and HOSI with tol=0.001 interpolation methods, in that order.

4.3.3 Discussion

From the experimental results in the Tables 4.1 and 4.2, we can see that the patch-based interpolation allows better reconstructions than those obtained with the pixel-based method. Regarding the comparison between cubic and linear interpolation within patches, we can see that the former produces only a very small improvement compared to linear interpolation. The per-

formance of the algorithms based on the proposed patches are close to those of the HOSI method [53] performed with tol=0.04; better results, instead, are obtained by performing HOSI with tol=0.001. However, it should be noted that the interpolation performed with the HOSI method (tol=0.001) brings better performance at the price of a much higher computational cost, as can be deduced from the Table 4.7, which shows the computational costs necessary to process the entire CT1 sequence by varying decimation factor M, for the various methods that have been compared.

M	SDI	PATCH-L	PATCH-C	HOSI (tol = 0.04)	HOSI (tol = 0.001)
2	78.334	32.878	89.715	40.981	3149.414
3	144.442	64.609	179.093	29.457	3541.816
4	216.174	100.851	269.580	24.399	3654.700
5	313.294	127.615	360.629	22.875	3705.462

Table 4.7: Computational costs (in seconds) obtained to process the CT1 sequence vs. the methods that are compared.

From the tables 4.3,4.4,4.5,4.6 it can be seen that all methods improve the quality of the 3D reconstruction that can be obtained from the LR sequence without any interpolation and that the quality decreases when the decimation factor increases. Finally it is evident that the ranking among the methods that can be derived from the observation of the 2D quality indexes is substantially confirmed by the results obtained with the 3D metrics. Concerning the results obtained using real sequences with a real low axial resolution, they clearly show that the quality of the reconstructions obtained from the original data (images in the first column of Fig. 4.12) is lower than those obtained using interpolated sequences (images in the columns from the second to the fourth of Fig. 4.12).

4.4 MRE sequence axial interpolation

MRE is an innovative acquisition technique which uses the propagation of mechanical shear waves in conjunction with an MRI technique to probe the elastic properties of in vivo tissues. Chapter 2 provides a detailed explanation of how this method operates and its possible applications. Measuring elasticity is of great interest since it allows both to differentiate the various physiological tissues and to distinguish healthy tissue from diseased ones; the greater rigidity of tissues, for example, may be related to a pathologi-

cal state. This method has been developed to investigate the properties of the liver affected by fibrosis and to evaluate the various stages associated with the pathology, in a non-invasive and reliable way; changes in the elastic properties of the liver tissue may be related to this pathology. In particular, the rigidity of the liver increases with the progression of the various stages of fibrosis. By combining the data obtained from this elastography analysis with a 3D reconstruction procedure from images, it is possible to obtain an anatomical 3D model with geometric and mechanical characteristics typical of the anatomical organ under examination. The limitation of the low resolution of the MRE leads to an inaccurate 3D with artifacts due to the low axial resolution. To solve this problem, the idea is to apply an interpolation along the axial direction to increase the slices sequence number and obtain a more accurate 3D reconstruction. In this case an MRE sequence (scanned with MR Touch GE Healthcare) of the liver with such characteristics, number of slices = 4, slices distance = 11 mm spatial resolution 256x256, was considered. The axial interpolation method was carried out by setting the subsampling factor M= 2 to have the same number of slices contained in the sequence MRI. The interpolated MRE sequence has been obtained by applying the PATCH-C method described in 4.2. After the interpolation process, different segmentations of the sequence were performed to simulate the elastography map and highlight the different tissue elasticity values. Figure 4.13 and 4.14 show the reconstruction of the 3D models corresponding to the original (low resolution) liver and to the interpolated sequence. Segmentation and 3D reconstruction are performed by using Materialise Mimics software. As can be seen, the reconstructed 3D model with the proposed method is much smoother than the model obtained from the original data in which *Lego* artifact is more prominent.

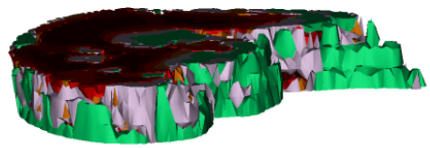

Figure 4.13: 3D MRE original liver model.

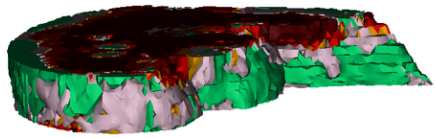

Figure 4.14: 3D MRE liver model reconstructed with PATCH-C method.

4.5 Concluding remarks

In this chapter we have investigated the problems related to the 3D reconstruction of anatomical models from low axial resolution tomographic sequences of diagnostic images. The acquisition of sequences by CT devices includes particular cases where the axial resolution that can be obtained is limited by the maximum allowed dose of ionizing radiation; this fact can lead to inaccurate 3D reconstructions. Both *pixel-based* and *patch-based* methods have been investigated. The comparison between the proposed methods has been performed using both objective and subjective criteria. The objective criteria considered include both radiometric (NRMSE of slices interpolated towards their reference) and geometric evaluation (mean and standard deviation of the 3D shape reconstruction error). These methods have also been compared with a highly sophisticated and performing algorithm of the literature [53]. The subjective criteria consider the segmentation accuracy of the interpolated slices and the low jerkiness of the reconstructed 3D shapes, calculated from radiometrically homogeneous segments. The results show that all axial interpolation methods are highly advantageous for the accuracy of the 3D model. The comparison between the *pixel-based* and *patch-based* approaches highlights the superiority of the latter. The comparison with the top performance benchmark [53] reveals that, although globally less accurate, due to the lack of adjustable parameters that determine the cost/performance trade-off, the proposed method seems to be slightly more accurate on a local basis, for example, in terms of maximum absolute radiometric error of the interpolated slices; at the same computational cost, also in terms of global error parameters, both radiometric and geometric. Real low axial resolution CT sequences are also used for a qualitative evaluation demonstrating that the proposed methods enable an effective slice interpolation and that the achievable 3D models clearly benefit from the increased axial

resolution. These results inspired the application of the proposed *patch-based* method on a MRE sequence.

Chapter 5

Multimodal fusion of biomedical images

In this chapter, the problem of biomedical image fusion is discussed. After a brief overview of image fusion in the biomedical field, a method inspired by remote sensing techniques is presented. The proposed fusion criterion aims to combine the main and complementary information extracted from the MRI and MRE, of the same patient, into a single image. The evaluation of the method is performed using quantitative metrics based on geometric and radiometric consistency and by visual inspection.

5.1 Introduction

The significant growth in the use of acquisition technologies in the medical field provides specialists with the opportunity to examine a series of images obtained with different imaging modalities and related to the same patient in order to make a more accurate and in-depth diagnosis. This is due to the fact that various acquisition methods generate images with different information content; for example, a morphological evaluation of the organs of interest can be performed from CT, MRI and US images, while the PET allows a functional analysis. By only evaluating images acquired through a single imaging method does not allow to capture all the necessary details to have an in-depth clinical picture and a consequent accurate diagnosis. For this reason, it is often necessary to compare side by side the various types of medical images. Normally, this comparison is the result of a mental act

of integration of the contents analyzed in the various images and consists of a mental superimposition of spatial information that can often be very difficult. As a consequence, multimodal medical imaging fusion plays a very important role in the field of medical imaging and is constantly growing. Multimodal medical images fusion is the process of combining and merging complementary information from images of the same subject obtained with different imaging modalities allowing a more accurate diagnosis and better treatment [83–85]. The automatic fusion of multimodal medical images is the topic of this chapter; more precisely, the registered images of MRI and MRE, acquired simultaneously on the same organs of a patient, are the imaging data acquisition modalities that are considered in this study. As already explained in chapter 2, MRE uses a highly sensitive phase contrast-based imaging method to analyze the propagation of shear waves in tissues subjected to harmonic mechanical excitation. The processing of acquired MRE data, allows the local value of the cutting modulus to be estimated, which yields images, usually in the form of color maps, showing the spatial distribution of the *elasticity* information of the tissue. The MRE acquisition process, on the other hand, does not allow information regarding the anatomical structures to be highlighted. To evaluate the elasticity of tissues there also exists another imaging method called Ultrasound Elastography (UE) that involves the use of an ultrasound probe producing acoustic pulses to evaluate the elastic modulus of the tissues with which it comes into contact. This diagnostic examination is less complex than MRE because it is easier to perform, but it is operator dependent and does not produce a tomographic sequence but only a two-dimensional image. In recent years, some MRI and UE image fusion works have been presented with the aim of improving the detection of tumors in different diagnostic contexts [86–88]; in this case the elasticity of a very restricted anatomical area is considered. On the contrary, the fusion of MRI and MRE images would make possible to obtain a final product, a fused MRE dataset, featuring both the high geometric content of the MRI and the elasticity information of the MRE, facilitating a more complete and accurate analysis on the whole anatomical part of the patient and allowing doctors to perform a more accurate investigation of the anatomical parts of interest. This is the core idea of the last part of this thesis work: to overcome the absence of spatial details typical of MRE images by means of fusion with higher spatial resolution MRI images. To this purpose, a novel fusion scheme, fully automated and based on Multiresolu-

tion analysis (MRA), is presented. Such fusion algorithm provides a good trade off between fusion performance, applicability to real-time situations, and preservation of the original medical relevance of MRE data.

5.2 Fusion of biomedical images: background

In the biomedical field, digital image fusion plays a very important role in several medical diagnosis and therapy applications. Over the years, extensive research on medical image fusion and a remarkable number of algorithms have been developed [83].
Image fusion techniques can be classified according to different criteria. One of the most common way to differentiate fusion algorithms is based on sensor homogeneity. The term *homogeneous image fusion* refers to the case in which the images to be merged are produced by sensors exploiting the same imaging mechanism. This category is also called *unimodal image fusion*. In remote sensing for Earth observation [89], the fusion of panchromatic and multispectral (MS) images, a.k.a. Pansharpening, is an example of homogeneous image fusion. The images subject to fusion are the outcome of measuring the reflected solar radiation of the scene, even though they are referred to different wavelengths and are characterized by different information content, also in terms of spatial resolution. On the other hand, *heterogeneous*, or *multimodal image fusion*, is referred to those cases in which the data to be merged come from sensors not sharing the same imaging mechanism. In the biomedical field, multimodal image fusion seems to be the most frequent case, also considering the demanding necessity of integrating as much complementary information as possible in order to support a better clinical outcome. Fusion of MRI-CT, MRI-PET, and MRI-US modalities are a few examples belonging to this category. An additional way to discriminate among fusion techniques is based on the content level subject to fusion, i.e., pixel level, feature level, and decision level [90]. Pixel level image fusion directly combines the pixels of the involved images in order to produce a new image, whereas feature level fusion aims to combine features extracted from the images to be merged. The extraction of the features can either be performed simultaneously on all the images or separately on each image. Finally, decision level fusion is the combination of the classification results performed individually on each image. In this case the fusion output is a classification map.
In the category of pixel level fusion, methods can further be classified ac-

cording to the adopted fusion approach.From a traditional image fusion perspective, two macro groups can be identified [91]: Component Substitution (CS) and Multiresolution Analyis (MRA). CS techniques, also referred to as *spectral methods*, aim at separating the spectral and spatial information of the images by means of specific spectral transformations. Examples of methods belonging to this class are the Intensity-Hue-Saturation (IHS), the Principal Component Analysis (PCA), and the Gram-Schmidt (GS) transform. MRA methods, or *spatial methods*, rely on a multiresolution decomposition of the images involved in the fusion, in order to extract spatial information from the image with higher spatial resolution and to inject it into the image with lower spatial resolution. Examples of MRA techniques are the decimated wavelet transform (DWT), the "Ã -trous" wavelet transform (ATWT), laplacian pyramids (LP), contourlet and curvelet transforms. These two basic classes can be enriched by taking into consideration several others methods that have been recently developed, such as those based on artificial neural networks (ANN), fuzzy-logic theory, Bayesian frameworks, and compressive Sensing [92, 93].

5.3 Proposed method

In this section, a fusion method aiming at combining pairs of MRI and MRE images is proposed. Let $\mathbf{I} = \{\mathbf{I}_k\}_{k=1,\dots,N}$ and $\mathbf{E} = \{\mathbf{E}_k\}_{k=1,\dots,M}$ be the sequences of MRI and MRE images, composed of N and M slices, respectively (N¿M); the objective is achieving fused MRE slices in which the elasticity information of the tissues, provided by the MRE, and the geometric information of the organs, provided by the MRI, are both present. Such a method can be classified as a solution to the multimodal image fusion problem. The characteristics of the images to be fused recall the problem of sharpening thermal infrared (TIR) images and MS images, typically encountered in remote sensing. In such a case, TIR images, which lack spatial details due to the blurring nature of the heat diffusion process, are sharpened by means of MS images - typically the bands in the visible and near-infrared regions (V-NIR) are used - that offer a richer geometric information content. Following this analogy, the MRE data could be thought as a TIR image that needs to be sharpened by means of the MRI, the corresponding V-NIR images in the thermal sharpening process. The proposed fusion algorithm takes into

consideration two desirable requirements that the ideal MRE fused dataset should have:

1. the details injected into the MRE should be an undistorted version of those present in the original MRI;

2. the radiometry of the original MRE should be preserved as much as possible.

In other words, spatial and radiometric distortions should be avoided. In the following sections, the various stages of the proposed method are described in detail.

5.3.1 Spatial and volumetric interpolation

As previously mentioned, MRE images provides information on elasticity of the investigated organ, allowing to evaluate its state of health without providing any information about its anatomical geometric structure. The lack of spatial details in the MRE images is due to the fact that the information on elasticity is obtained through a wave propagation in the tissues induced by a vibrating driver that is placed on the patient's body during the MRI examination. This movement, acting as a motion blurring, is the main responsible of the coarser spatial resolution of MRE images, if compared to MRI images. In image fusion, whenever images with different resolution are involved, spatial interpolation of the lower resolution image to the scale of the higher resolution one, is the first necessary step of the process. In this case, in order to overcome the different pixel size of the two sequences, a bicubic interpolation of the MRE images is performed at the desired MRI scale, in order to have pixel by pixel superimposable sequences. The MRE images investigated in the simulations have pixel size twice as large as of that of MRI images. Moreover, they all have been acquired during the same examination, resulting into an axially aligned dataset, which will not require any additional coregistration operation. Another aspect to be considered, involves the different number of slices present in the two sequences; typically, MRE sequences are characterized by a lower number of slices than MRI sequences. This is due to the more strict requirements imposed to the patients by the elastographic acquisition process. In fact, elastrography imaging requires patients to hold their breaths during the whole acquisition, which obviously set a time limitation leading to a limited number of

acquirable elastrographic slices. Typically, MRE sequences are created by prescribing on the coronal plane four slices in axial section, one for each expiratory apnea, acquired during the final phase of exhalation and positioned so as to include the largest transverse dimension of the liver. In order to have MRI and MRE sequences with the same number of slices, an axial interpolation strategy is applied. The importance of this step is reflected into the fact that the subsequent fusion process will be performed on a slice-by-slice basis, which ultimately will allow doctors to perform a more accurate and complete medical evaluation. The axial interpolation scheme, applied to the MRE dataset, is shown in Fig. 5.1. An interpolation based on the DVF

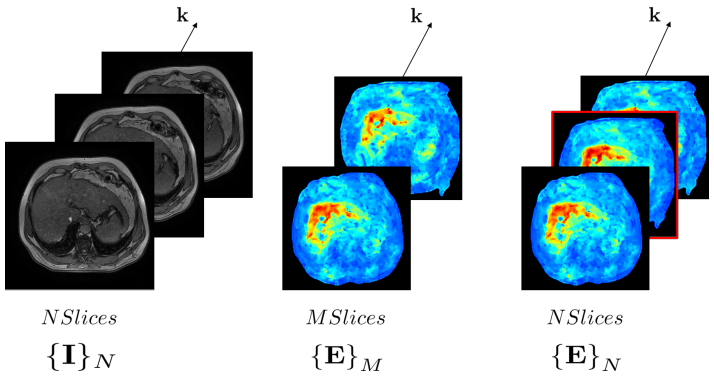

Figure 5.1: Volumetric interpolation of MRE sequence. From right to left: MRI sequnce composed by N slices, original MRE sequence composed by M slices, interpolated MRE sequence composed by N slices.

estimation, between two adjacent slices, was performed to improve the axial spatial resolution of the MRE sequence. The DVF was then processed using a WVMF and used to estimate the intermediate sections between those available. The interpolation method considered is the one presented in 4.2.3 and indicated as PATCH-C. As a result of volumetric interpolation, MRE and MRI share the same dimensionality of the slices and therefore the fusion process can take place between each pair of axially aligned MRE-MRI slices. Applying the fusion method to each pair of axially aligned slices results in a final sequence characterized by images in which both the elasticity information of the tissues and the geometric information of the organs are present. Hereinafter, for notation simplicity, k index is dropped.

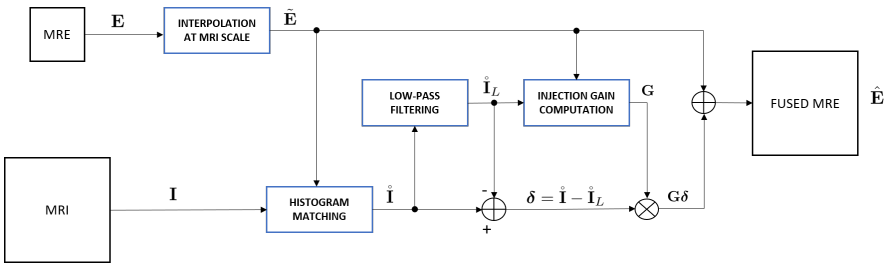

Figure 5.2: Flowchart detailing the steps of the proposed fusion method.

5.3.2 histogram-matching operation

The fusion scheme, proposed in this work, belongs to the MRA class and its complete flowchart is reported in Figure 5.2. The flowchart depicts the fusion between the pair of kth MRE and MRI slices, subsequent to the volumetric interpolation of the MRE dataset. The first step of the scheme include the histogram matching operation. With the term histogram matching [94], we refer to the equalization of the first-order statistics, mean and variance, between the images to be fused. This step, often overlooked in image fusion, is particular important whenever the images to be merged are characterized either by different radiometric resolutions, i.e., number of bits, or different radiometric formats, such as digital numbers (DN) or physical quantities (i.e., kPa). Such an operation guarantees a radiometric normalization of the data, which represents an essential prerequisite for high fusion performance. The histogram matching operation may be written as:

$$\mathring{\mathbf{I}} = (\mathbf{I} - \mu_{\mathbf{I}}) \cdot \frac{\sigma_{\tilde{\mathbf{E}}}}{\sigma_{\mathbf{I}}} + \mu_{\tilde{\mathbf{E}}} \tag{5.1}$$

in which μ and σ are mean and standard deviation, respectively.

5.3.3 Injection gain computation

The histogram-matched version of the MRI is filtered by a low-pass filter in order to extract the geometric details $\boldsymbol{\delta}$ defined as:

$$\boldsymbol{\delta} = \mathring{\mathbf{I}} - \mathring{\mathbf{I}}_L \tag{5.2}$$

where $\mathring{\mathbf{I}}_L$ is the low pass histogram-matched MRI. After extracting the geometric information from the MRI, the following additive detail injection

fusion scheme is employed to generate the fused image:

$$\hat{\mathbf{E}} = \tilde{\mathbf{E}} + \mathbf{G}\left(\mathring{\mathbf{I}} - \mathring{\mathbf{I}}_L\right) \ . \tag{5.3}$$

Equation 5.3 shows that the fused MRE image $\hat{\mathbf{E}}$ is obtained by adding to the interpolated slice $\tilde{\mathbf{E}}$ the geometric details, after the modulation by a suitable *injection gain*, $\mathbf{G}$. About the choice of the injection gain, which suitably weighs the detail content to be injected into the MRE, multiple strategies may be devised. In this regard, we make use of the Gram-Schmidt orthogonalization procedure [95], providing the following closed-form expression for the injection gain:

$$\mathbf{G} = \frac{\mathrm{cov}(\tilde{\mathbf{E}}, \mathbf{I}_L)}{\mathrm{var}(\mathbf{I}_L)}. \tag{5.4}$$

Such an injection coefficient is usually referred to as *projective coefficient*, since it is the modulus of the projected vector of the $\tilde{\mathbf{E}}$ along $\mathbf{I}_L$.The more general formulation of the projection coefficient derived from Gram-Schmidt orthogonalization [95] is defined in terms of inner products. We replaced inner products with covariances and variances assuming to deal with Euclidean zero-mean vectors. The gain represents the key point of GS spectral sharpening [96,97], one of the most successful first-generation Pansharpening methods. By definition, the projection coefficient defined in Equation 5.4 is a scalar term; conversely, we specifically used a matrix notation to indicate our choice to use a locally space-varying injection coefficient, computed on a sliding window of 16×16 pixels. With simple algebraic manipulations, Equation 5.4 can be rewritten as:

$$\mathbf{G} = \mathrm{CC}(\tilde{\mathbf{E}}, \mathbf{I}_L) \cdot \sqrt{\frac{\mathrm{var}(\tilde{\mathbf{E}})}{\mathrm{var}(\mathbf{I}_L)}}. \tag{5.5}$$

where CC is the linear correlation coefficient. In the presented fusion framework, $\mathbf{G}$ plays a key role since determines whether the detail is to be injected or not, and if so on what proportion, based on local correlation between the two images. The fact that the proposed method belongs to the multi-resolution analysis class can be deduced from the detail expression in Equation 5.3. In fig.5.3, by way of example, the injection gain and the spatial details computed by the proposed algorithm for a given pair of MRI and MRE images are shown.

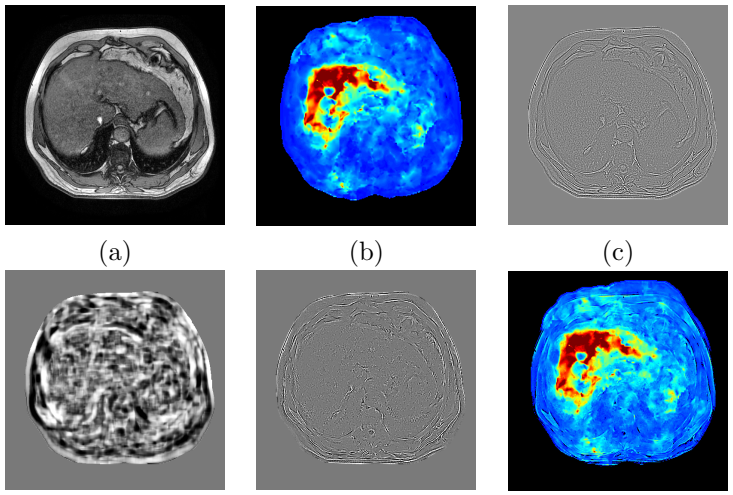

Figure 5.3: (a): MRI image; (b) expanded MRE image; (c): spatial details δ; (d) injection gain $\mathbf{G}$; (e) product of injection gain and spatial details $\mathbf{G} \cdot \delta$, (f) fused image.

5.4 Experimental results

In this section the fusion experimental results will be presented. Two image datasets, both comprising MRI and MRE sequences and featuring the liver anatomy and elasticity respectively, have been tested. The dataset has been acquired by the 1.5 T unit (HD Signa Exciting machine GE Medical System, Wis, USA) and the MR TOUCH system (GE Medical System, Wis, USA). The two datasets, referred to as **Patient1** and **Patient2** in the following, are composed of 7 T1 MRI and 4 MRE slices (which are axially interpolated to obtain 7 slices). The original MRE images have radiometric resolution of 15-bit, slice spacing of 10.5 mm, thickness of 8 mm and a size of 256×256 pixels, whereas the MRI images have radiometric resolution of 12-bit, slices spacing of 6 mm, thickness of 5 mm and a size of 512×512 pixels. During the experimentation phase, three algorithms based on the fusion scheme described in 5.3 were tested: in the first one, the detail is injected without undergoing any modeling process, in the second one, the injection detail is modeled using a global gain, in the third one, the detail is

modeled using a local gain; the three methods are referred as ADM, ADM-GG, ADM-LG respectively. The performance of the proposed fusion method will be evaluated along with other two state-of-the-art methods: the Gradient Transfer Fusion (GTF) method [98], and the ATWT method [97]. The former is based on gradient transfer and total variation (TV) minimization and was proposed for Infrared and Visible image fusion, whereas the latter is a successful MRA algorithm. The GTF requires to set the regularization parameter, λ. We carefully chose such a parameter maximizing the overall performance for each dataset, resulting in $\lambda = 0.85$ and $\lambda = 1.65$, for the **Patient1** and **Patient2** datasets, respectively.

5.4.1 Performance assessment

Quality evaluation of image fusion products has been, and still is, the object of extensive researches. The problem is complicated by the fact that it may not be easy to formalize what "quality" means in the fusion process. In this regard, a protocol of assessment should have very clear objectives and possibly require a reference on which the comparison relies [99]. Image fusion assessment is traditionally performed in two ways: (1) human visual inspection by a panel of investigators, (2) mathematical functions capable of measuring or inferring the similarity of the fusion product to a reference target, which is always unavailable and often also undefined. In this thesis work, the latter approach is pursued. In remote sensing image fusion, especially multispectral pansharpening applications, quality assessment is performed following the Wald's protocol [100, 101], which substantially requires the fused image to satisfy two main properties:

- *consistency:* the fused image, once spatially degraded to the original resolution, should be as close as possible to the original image;

- *synthesis:* any LR image fused by means of a HR image should be as identical as possible to the ideal image that the corresponding sensor, if existent, would observe at the resolution of the HR image.

The property of consistency is usually easier to assess, since the original LR image can be used as a reference. Only the procedure of spatial degradation and the matching function are to be standardized. On the contrary, the synthesis property is harder to be verified, since a reference is required. A viable shortcoming stems from the assumption of scale-invariance of the

scene, that is, quality measures do not vary with the resolution, at which the scene is imaged. This allows the quality to be measured at a resolution lower than the original one, for which the reference image is available. More specifically, the process consists of spatially degrading both the enhancing and the enhanced datasets by a factor equal to the scale ratio between them and using the original LR image as reference. Obviously, such an assumption is not always valid, especially when the degradation process does not mimic the actual sensor acquisition process. In the case of multi-modal image fusion, the applicability of the synthesis properties of the Wald's protocol is questionable since a multi-modal fusion method aims at producing images in which the features coming from different sensors should in principle be both present. If the imaging sensors exploit different physical mechanisms, e.g., reflectivity and emissivity in the case of fusion of optical and thermal data, the assumption that an "ideal" sensor producing the fused image could exist is unlikely, since such a sensor should be able to measure and integrate different physical phenomena at the same time. This fact impairs the possibility of evaluating the synthesis properties at a reduced scale. In other words, when fusion of heterogeneous data is concerned, in the context of Wald's protocol the sole suitable choice for evaluating quality is consistency [102]. Unfortunately, Wald's protocol does not include a spatial, or geometric, consistency property, since the spatial quality is implicit in the synthesis property. To give a better insight of the problem, we split the consistency property into two terms, which are given here with reference to our MRI-MRE fusion problem:

- *radiometric consistency:* the fused MRE image, once spatially degraded at the original scale, should be as close as possible to the original MRE image, i.e., the source of the radiometric information;

- *geometric consistency:* the local similarity relationships between the original MRE and a spatially degraded version of MRI should be retained by the fused MRE and the original enhancing MRI. This is the rationale of the spatial quality index of the QNR protocol [103].

Radiometric and geometric consistency are evaluated by using the following three metrics (the first two referring to radiometric consistency, the third to geometric consistency).

Normalized Root Mean Square Error (NRMSE)

$$\text{NRMSE} \triangleq \frac{\sqrt{E[(\tilde{\mathbf{E}} - \hat{\mathbf{E}}^{lp})^2]}}{\mu_{\hat{\mathbf{E}}^{lp}}} \tag{5.6}$$

where $E[\cdot]$ represents the expectation operator, approximated by means of a spatial average and $\hat{\mathbf{E}}^{lp}$ indicates the fused low-pass filtered MRE slice. NRMSE is a distortion index, hence its ideal value is zero. Note that (5.6) is the restriction to single-band data of the ERGAS index, originally introduced by L. Wald [99], and widespread for assessment of pansharpened products [97].

Radiometric Universal Image Quality Index (Q_R)

$$\text{Q}_\text{R} = \frac{1}{B} \sum_b \text{Q}(\tilde{\mathbf{E}}_b, \hat{\mathbf{E}}_b^{lp}, B) \tag{5.7}$$

where Q is the Universal Image Quality Index defined as [104]:

$$\text{Q}(A, B) \triangleq \frac{4\sigma_{A,B} \cdot \mu_A \cdot \mu_B}{(\sigma_A^2 + \sigma_B^2)[\mu_A^2 + \mu_B^2]} \tag{5.8}$$

with $\sigma_{A,B}$ denotes the covariance between A and B. In (5.7), $\mathbf{E}_b$ and $\hat{\mathbf{E}}_b^{lp}$ denote non overlapped blocks of N×N pixels (in the implementation, was used N = 16); B indicates the number of blocks composing the image. Q measures the similarity between two images and thus its ideal value is one. Incidentally, (5.7) is the restriction of the spectral quality index proposed by Khan *et al.* [105] to single-band image data.

Geometric Universal Image Quality Index (Q_G)

$$\text{Q}_\text{G} = 1 - \left[\frac{1}{B} \sum_b |\text{Q}(\hat{\mathbf{E}}_b, \mathbf{I}_b) - \text{Q}(\tilde{\mathbf{E}}_b, \mathbf{I}_b^{lp})| \right] \tag{5.9}$$

where $\mathbf{I}^{lp}$ denote the low-pass filtered MRI and subscript b defines the bth block. The statistics are calculated locally over non overlapped blocks of 16×16 pixels and then the global measure is obtained by averaging over the whole image. Eq. (5.9) is nothing else than the restriction of the spatial QNR index [103] to single-band data. The coupling of the aforementioned indexes

has been originally proposed for full-scale assessment of pansharpening fusion [106]. The calculation of both the indexes requires a low-pass digital filter for the spatial degradation. To this end, we used a Gaussian filter [107], whose frequency response is shown in Figure 5.4.

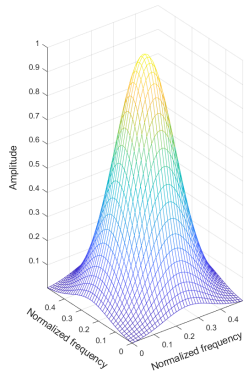

Figure 5.4: Frequency responses of the digital filter employed in the quality assessment procedure.

5.4.2 Fusion experiments

Tables 5.1 and 5.2 show the results of the quality assessment for **Patient1** and **Patient2**, respectively. Tables show results in terms of average NRMSE, QR and QG on the slices just generated, using ADM, ADM-GG and ADM-LG methods. In both are also reported the metrics values obtained with the Gradient Transfer Fusion (GTF) method [98], and the á trous wavelet transform (ATWT) method [108] .

	NRMSE	$\mathbf{Q}_R$	$\mathbf{Q}_G$
Ideal	0	1	1
ADM	0.0371	0.9019	0.8876
ADM-GG	0.0200	0.9695	0.9519
ADM-LG	0.0191	0.9739	0.9988
GTF	0.0925	0.6951	0.7485
ATWT	0.0830	0.7345	0.7602

Table 5.1: Fusion assessment for the **Patient1** dataset.

	NRMSE	$\mathbf{Q}_R$	$\mathbf{Q}_G$
Ideal	0	1	1
ADM	0.0287	0.8925	0.9257
ADM-GG	0.0168	0.9285	0.9685
ADM-LG	0.0155	0.9346	0.9993
GTF	0.1237	0.6421	0.7207
ATWT	0.0739	0.7730	0.8219

Table 5.2: Fusion assessment for the **Patient2** dataset.

Figure 5.5 and Figure 5.6 show the fusion results for the **Patient1** and **Patient2** datasets, respectively. For each dataset, original and fused images by using ADM-LG, GTF and ATWT methods are shown.

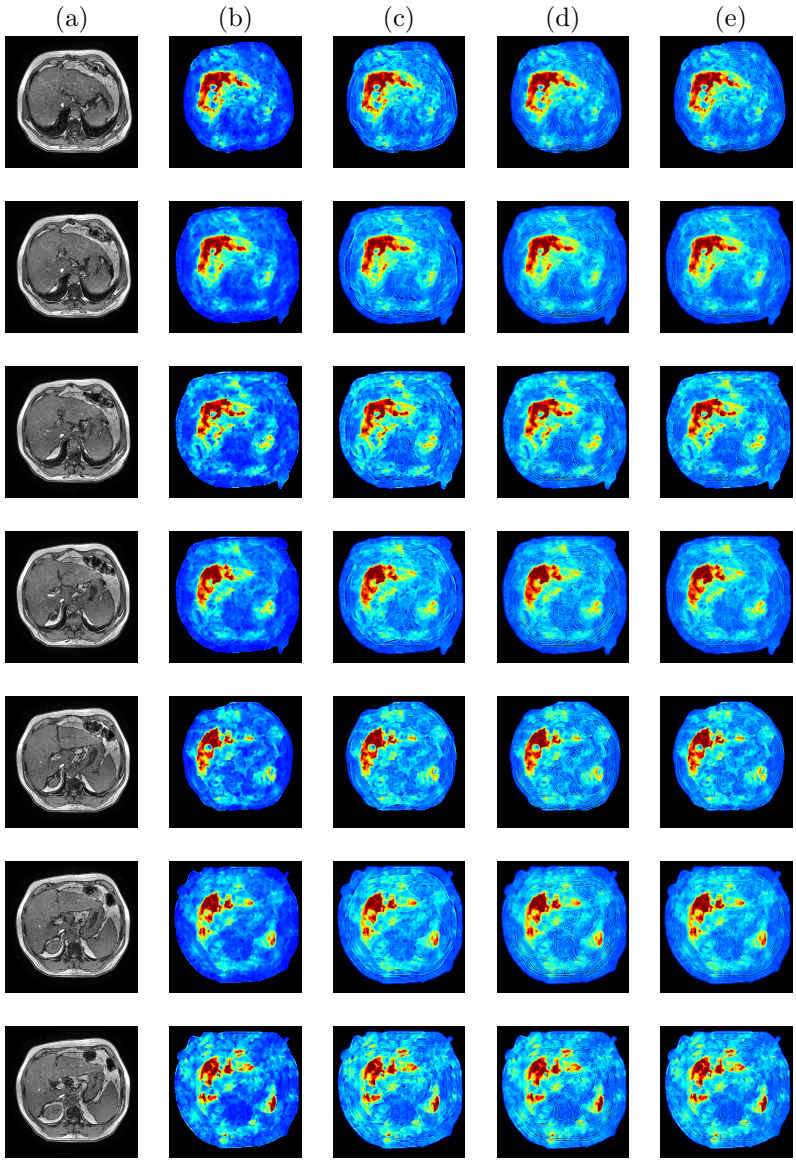

Figure 5.5: Fusion results for the **Patient1** dataset. Each row is related to a specific slice, $k = 1, ..., 7$. Columns are organized as follows:(a) original T1 MRI; (b) expanded MRE; (c) ADM-LG; (d) GTF; (e) ATWT.

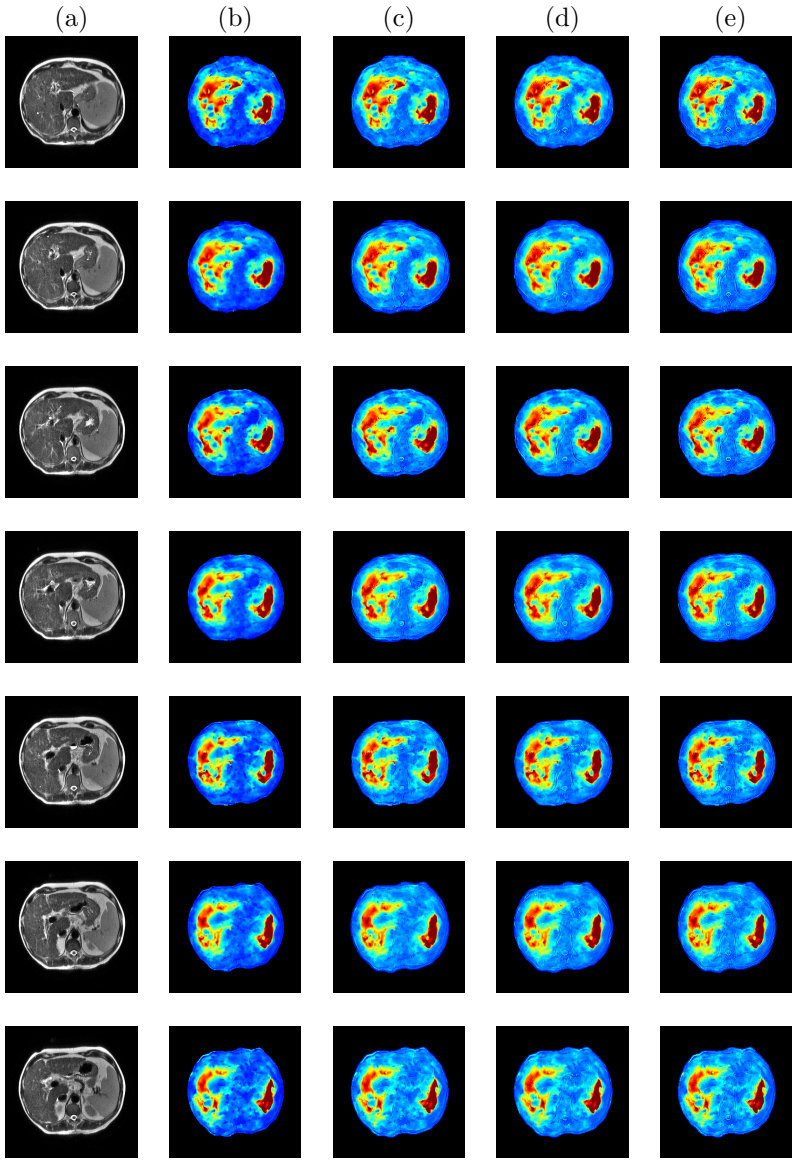

Figure 5.6: Fusion results for the **Patient2** dataset. Each row is related to a specific slice, $k = 1, ..., 7$. Columns are organized as follows: (a) original T1 MRI; (b) expanded MRE; (c) ADM-LG; (d) GTF; (e) ATWT.

5.5 Concluding remarks

In the biomedical field, using different types of imaging allows multiple anatomical information to be obtained from the same patient because each type of imaging only highlights specific anatomical information. The problem for the physician is to combine information from different images, which is often done mentally and is therefore very complex and difficult. One solution is to combine different images of the same subject. In this chapter we have investigated the problem of the fusion of MRI and MRE images. methods based on detail modulation calculated on a local and global basis were investigated. The comparison between the proposed methods has been performed using both quantitative metrics and visual inspection. The objective criteria considered include both radiometric and geometric consistency evaluation. Regarding the former, NRMSE and Q_R, of original MRE towards low-pass fused MRE, are computed. The geometric consistency has been evaluated by computing Q_G. The results show that all methods generate fused images characterized by consistency values very close to the ideal ones. Two methods proposed in the literature, one based on the gradient and the other based on the wavelet transform, were used as a benchmark. This comparison shows that the proposed methods are superior in terms of both radiometric and geometric maximum error. Visual inspection of the fused images shows that the radiometric information is very close to that contained in the original MRE and that the geometric detail is not a distorted version of the original MRI.

Chapter 6

Conclusions

The three-dimensional reconstruction of anatomical models plays a fundamental role in biomedical field, especially in preoperative planning and surgical training. These models are used as a basis for pre-operative studies since they faithfully reproduce the patient's anatomy, providing surgeons with a real perception of the scenario under examination and of the surrounding structures. The Physical interaction between the model and the surgeon also allows the surgery before entering the operating room using various surgical instruments, to be simulated. In this way, it is possible to understand difficulties in advance, anatomical conditions and different depths and lengths of surgical instruments, to predict critical points of intervention and to identify appropriate surgical strategies, with the clear advantage of reducing operating times and surgical errors. During this thesis work, a general pipeline was developed to produce a patient-specific 3D anatomical model to help surgeon in the pre-operative planning process. The pipeline considers different production methods that can be used according to the challenge and goal of preoperative planning but are also strictly dependent on the specific pathological case. Experience with the neurosurgery team of the Meyer Children's Hospital in Florence is reported; this involved the use of four 3D printed models to plan surgical interventions according to the proposed pipeline. The 3D model reconstruction process may involve the use of advanced image processing methods in order to improve the anatomical accuracy of the final reconstructed product. In fact, in some cases only low axial resolution sequences are available, so that the reconstructed model is characterised by artifacts and inaccurate anatomical geometry. One possi-

ble way to solve this problem is to use axial interpolation algorithms that allow to increase the axial resolution by generating intermediate slices from two adjacent ones within the same sequence. In this thesis work, problems related to the 3D reconstruction of anatomical models from tomographic sequences of diagnostic images with low axial resolution were investigated and two axial interpolation methods based on displacement vector field estimation were proposed: one pixel-based and one patch-based. The assessment of the proposed methods was carried out considering a sequence of CT images of the skull. This sequence was decimated to obtain a low-resolution synthetic one which was axially interpolated using the proposed methods and varying the interpolation factor. The proposed methods were evaluated considering both radiometric and geometric quality. In the first case, NRMSE of slices interpolated towards their reference was evaluated, in the second case, 3D models were first reconstructed from both the original and the reconstructed sequence and then the mean and standard deviation of the 3D shape reconstruction error were calculated. The results show that although the patch-based method is preferable to the pixel-based one, both are highly advantageous for the geometric accuracy of the 3D model. The comparison with other methods taken from the literature reveals that the proposed method, although less accurate globally, seems to be slightly more accurate on a local basis, e.g., in terms of absolute maximum radiometric error of slices at the price of a much higher computational cost. The proposed methods have been also applied to two cases of real sequences with low axial resolution, CT acquisition on neonatal patients and MRE, demonstrating in both cases that accurate 3D reconstructions can be obtained. During this thesis work, the problem of medical image fusion was also investigated. A method for the fusion of MRE and MRI images was developed with the aim of generating a single MRE fused image containing the geometrical detail of the MRI and the elasticity information of the MRE. The proposed method belongs to the class of Multiresolution Analyis (MRA) methods and has been developed considering two fundamental requirements: the details injected into the MRE should be an undistorted version of those present in the original MRI and the radiometric information of the original MRE should be preserved as much as possible. Based on the proposed fusion scheme three algorithms were tested by varying the details modulation. The assessment of the methods was carried out quantitatively by considering radiometric and geometric consistency using appropriate quality indices. The results

show that all methods generate fused images in which the consistency values considered are close to the ideal ones. These methods were compared with two methods proposed in the literature and results show that proposed methods are superior in terms of both maximum radiometric and geometric error. In addition, a visual inspection of the fused images shows that the original radiometric information is preserved and that the geometric detail is an undistorted version of that present in the original MRI images.

Bibliography

[1] A. Murphy and F. Gaillard. Mri sequences (overview). [Online]. Available: https://radiopaedia.org/articles/mri-sequences-overview

[2] Y. K. Mariappan, K. J. Glaser, and R. L. Ehman, "Magnetic resonance elastography: a review," *Clin. Anat.*, vol. 23, no. 5, pp. 497–511, 2010.

[3] L. V. Hiscox, C. L. Johnson, E. Barnhill, M. D. McGarry, J. Huston 3rd, E. J. Van Beek, J. M. Starr, and N. Roberts, "Magnetic resonance elastography (mre) of the human brain: technique, findings and clinical applications," *Phys. Med. Biol.*, vol. 61, no. 24, p. R401, 2016.

[4] M. C. Murphy, J. Huston, K. J. Glaser, A. Manduca, F. B. Meyer, G. Lanzino, J. M. Morris, J. P. Felmlee, and R. L. Ehman, "Preoperative assessment of meningioma stiffness using magnetic resonance elastography," *J. Neurosurg.*, vol. 118, no. 3, pp. 643–648, 2013.

[5] A. L. McKnight, J. L. Kugel, P. J. Rossman, A. Manduca, L. C. Hartmann, and R. L. Ehman, "Mr elastography of breast cancer: preliminary results," *AJR Am. J. Roentgenol.*, vol. 178, no. 6, pp. 1411–1417, 2002.

[6] M. Lev and R. Gonzalez, "17 - ct angiography and ct perfusion imaging," in *Brain Mapping: The Methods*, A. W. Toga and J. C. Mazziotta, Eds. San Diego: Academic Press, 2002, pp. 427 – 484.

[7] C. Westbrook and J. Talbot, *MRI in Practice*. John Wiley & Sons, 2018.

[8] V. P. Grover, J. M. Tognarelli, M. M. Crossey, I. J. Cox, S. D. Taylor-Robinson, and M. J. McPhail, "Magnetic resonance imaging: principles and techniques: lessons for clinicians," *J. Clin. Exp. Hepatol.*, vol. 5, no. 3, pp. 246–255, 2015.

[9] P. Sprawls, *Magnetic resonance imaging: principles, methods, and techniques*. Medical Physics Publishing Madison, WI, 2000.

[10] D. Miller, P. Rudge, G. Johnson, B. Kendall, D. Macmanus, I. Moseley, D. Barnes, and W. McDonald, "Serial gadolinium enhanced magnetic resonance imaging in multiple sclerosis," *Brain*, vol. 111, no. 4, pp. 927–939, 1988.

[11] G.-H. Jahng, K.-L. Li, L. Ostergaard, and F. Calamante, "Perfusion magnetic resonance imaging: a comprehensive update on principles and techniques," *Korean J. Radiol.*, vol. 15, no. 5, pp. 554–577, 2014.

[12] H. Zhu and P. B. Barker, "Mr spectroscopy and spectroscopic imaging of the brain," in *Magnetic resonance neuroimaging.* Springer, 2011, pp. 203–226.

[13] B. Biswal, F. Zerrin Yetkin, V. M. Haughton, and J. S. Hyde, "Functional connectivity in the motor cortex of resting human brain using echo-planar mri," *Magnet. Reson. Med.*, vol. 34, no. 4, pp. 537–541, 1995.

[14] W. A. Weber, "Positron emission tomography as an imaging biomarker," *J. Clin. Oncol.*, vol. 24, no. 20, pp. 3282–3292, 2006.

[15] H. T. Banks, S. Hu, and Z. R. Kenz, "A brief review of elasticity and viscoelasticity for solids," *Adv. Appl. Math. Mech.*, vol. 3, no. 1, pp. 1–51, 2011.

[16] R. Muthupillai, D. Lomas, P. Rossman, J. F. Greenleaf, A. Manduca, and R. L. Ehman, "Magnetic resonance elastography by direct visualization of propagating acoustic strain waves," *science*, vol. 269, no. 5232, pp. 1854–1857, 1995.

[17] A. Manduca, T. E. Oliphant, M. A. Dresner, J. Mahowald, S. A. Kruse, E. Amromin, J. P. Felmlee, J. F. Greenleaf, and R. L. Ehman, "Magnetic resonance elastography: non-invasive mapping of tissue elasticity," *Med. Image Anal.*, vol. 5, no. 4, pp. 237–254, 2001.

[18] T. E. Oliphant, J. L. Mahowald, R. L. Ehman, and J. F. Greenleaf, "Complex-valued quantitative stiffness estimation using dynamic displacement measurements and local inversion of conservation of momentum," in *1999 IEEE Int. Ultrason. Symp.*, vol. 2. IEEE, 1999, pp. 1641–1644.

[19] M. Yin, J. A. Talwalkar, K. J. Glaser, A. Manduca, R. C. Grimm, P. J. Rossman, J. L. Fidler, and R. L. Ehman, "Assessment of hepatic fibrosis with magnetic resonance elastography," *Clin. Gastroenterol. H.*, vol. 5, no. 10, pp. 1207–1213, 2007.

[20] T. D. Ngo, A. Kashani, G. Imbalzano, K. T. Nguyen, and D. Hui, "Additive manufacturing (3d printing): A review of materials, methods, applications and challenges," *Compos. B. Eng.*, vol. 143, pp. 172–196, 2018.

[21] B. L. Tai, D. Rooney, F. Stephenson, P.-S. Liao, O. Sagher, A. J. Shih, and L. E. Savastano, "Development of a 3d-printed external ventricular drain placement simulator," *J. Neurosurg.*, vol. 123, no. 4, pp. 1070–1076, 2015.

[22] M. Oishi, M. Fukuda, N. Yajima, K. Yoshida, M. Takahashi, T. Hiraishi, T. Takao, A. Saito, and Y. Fujii, "Interactive presurgical simulation applying advanced 3d imaging and modeling techniques for skull base and deep tumors," *J. Neurosurg.*, vol. 119, no. 1, pp. 94–105, 2013.

[23] V. Waran, V. Narayanan, R. Karuppiah, S. L. Owen, and T. Aziz, "Utility of multimaterial 3d printers in creating models with pathological entities to enhance the training experience of neurosurgeons," *J. Neurosurg.*, vol. 120, no. 2, pp. 489–492, 2014.

[24] A. Tejo-Otero, I. Buj-Corral, and F. Fenollosa-Artés, "3d printing in medicine for preoperative surgical planning: A review," *Ann. Biomed. Eng.*, vol. 48, no. 2, pp. 536–555, 2020.

[25] V. Mamone, R. M. Viglialoro, F. Cutolo, F. Cavallo, S. Guadagni, and V. Ferrari, "Robust laparoscopic instruments tracking using colored strips," in *International Conference on Augmented Reality, Virtual Reality and Computer Graphics*. Springer, 2017, pp. 129–143.

[26] E. Nocerino, F. Remondino, F. Uccheddu, M. Gallo, and G. Gerosa, "3d modelling and rapid prototyping for cardiovascular surgical planning-two case studies." *ISPRS Archives*, vol. 41, 2016.

[27] C. C. Ploch, C. S. Mansi, J. Jayamohan, and E. Kuhl, "Using 3d printing to create personalized brain models for neurosurgical training and preoperative planning," *World Neurosurg.*, vol. 90, pp. 668–674, 2016.

[28] A. Ottlakan, B. Borda, Z. Morvay, A. Maraz, and J. Furak, "The effect of diagnostic imaging on surgical treatment planning in diseases of the thymus," *Contrast Media Mol. Imaging*, vol. 2017, 2017.

[29] S. Grau, S. Kellermann, M. Faust, M. Perrech, D. Beutner, A. Drzezga, and J. Zöller, "Repair of cerebrospinal fluid leakage using a transfrontal, radial adipofascial flap: an individual approach supported by three-dimensional printing for surgical planning," *World Neurosurg.*, vol. 110, pp. 315–318, 2018.

[30] D. Hoang, D. Perrault, M. Stevanovic, and A. Ghiassi, "Surgical applications of three-dimensional printing: a review of the current literature & how to get started," *Ann. Transl. Med.*, vol. 4, no. 23, 2016.

[31] A. Pelagotti, A. Del Mastio, F. Uccheddu, and F. Remondino, "Automated multispectral texture mapping of 3d models," in *Eur. Signal Process. Conf.* IEEE, 2009, pp. 1215–1219.

[32] M. A. Viergever, J. A. Maintz, S. Klein, K. Murphy, M. Staring, and J. P. Pluim, "A survey of medical image registration–under review," 2016.

[33] S. Miao, Z. J. Wang, and R. Liao, "A cnn regression approach for real-time 2d/3d registration," *IEEE Trans. Med. Imaging*, vol. 35, no. 5, pp. 1352–1363, 2016.

[34] D. L. Hill, P. G. Batchelor, M. Holden, and D. J. Hawkes, "Medical image registration," *Phys. Med. Biol.*, vol. 46, no. 3, p. R1, 2001.

[35] P. J. Besl and N. D. McKay, "Method for registration of 3-d shapes," in *P. Soc. Photo-Opt. Ins.*, vol. 1611. International Society for Optics and Photonics, 1992, pp. 586–606.

[36] Q.-Y. Zhou, J. Park, and V. Koltun, "Fast global registration," in *Comput. Vis. ECCV*. Springer, 2016, pp. 766–782.

[37] D.-Y. Chen and M. Ouhyoung, "A 3d model alignment and retrieval system," in *Proceedings of international computer symposium, workshop on multimedia technologies*, vol. 2. Hualien, Taiwan, 2002, pp. 1436–1443.

[38] T. M. Bücking, E. R. Hill, J. L. Robertson, E. Maneas, A. A. Plumb, and D. I. Nikitichev, "From medical imaging data to 3d printed anatomical models," *PloS one*, vol. 12, no. 5, p. e0178540, 2017.

[39] M. A. Balafar, A. R. Ramli, M. I. Saripan, and S. Mashohor, "Review of brain mri image segmentation methods," *Artif. Intell. Rev.*, vol. 33, no. 3, pp. 261–274, 2010.

[40] E. Ebel and T. Sinnemann, "Fabrication of fdm 3d objects with abs and pla and determination of their mechanical properties," *RTejournal*, vol. 2014, no. 1, 2014.

[41] F. Buonamici, M. Carfagni, R. Furferi, L. Governi, M. Saccardi, and Y. Volpe, "Optimizing fabrication outcome in low-cost fdm machines. part 1-metrics," *Manuf. Technol*, vol. 18, no. 3, pp. 372–378, 2018.

[42] J. S. Witowski, M. Pedziwiatr, P. Major, and A. Budzynski, "Cost-effective, personalized, 3d-printed liver model for preoperative planning before laparoscopic liver hemihepatectomy for colorectal cancer metastases," *Int. J. Comput. Assist Radiol. Surg.*, vol. 12, no. 12, pp. 2047–2054, 2017.

[43] E. Mussi, R. Furferi, Y. Volpe, F. Facchini, K. S. McGreevy, and F. Uccheddu, "Ear reconstruction simulation: from handcrafting to 3d printing," *Bioeng.*, vol. 6, no. 1, p. 14, 2019.

[44] K. Bootsma, E. Dimbath, J. Berberich, and J. L. Sparks, *Materials Used as Tissue Phantoms in Medical Simulation.* Springer Berlin Heidelberg, 2016, pp. 1–48.

[45] C.-C. Kuo and M.-Y. Lai, "Development of an automatic vacuum degassing system and parameters optimization for degassing process," *Indian J. Eng. Mater. Sci.*, vol. 18, pp. 405–410, 2011.

[46] S. Nagaraja, P. Anslow, and B. Winter, "Craniosynostosis," *Clin. Radiol.*, vol. 68, no. 3, pp. 284–292, 2013.

[47] M. Vannier, C. Hildebolt, J. Marsh, T. Pilgram, W. McAlister, G. Shackelford, C. Offutt, and R. Knapp, "Craniosynostosis: Diagnostic value of

three-dimensional CT reconstruction," *Radiology*, vol. 173, no. 3, pp. 669–673, 1989.

[48] K. Kutanzi, A. Lumen, I. Koturbash, and I. Miousse, "Pediatric exposures to ionizing radiation: Carcinogenic considerations," *Int. J. Environ. Res. Public Health*, vol. 13, no. 11, pp. 1–14, 2016.

[49] M. Toossi, B. Taghi, and M. Malekzadeh, "Radiation dose to newborns in neonatal intensive care units," *Iran. J. Radiol.*, vol. 9, no. 3, pp. 145–149, 2012.

[50] S. Binaghi, F. Gudinchet, and B. Rilliet, "Three-dimensional spiral CT of craniofacial malformations in children," *Pediatr. Radiol.*, vol. 30, no. 12, pp. 856–860, 2000.

[51] A. Goshtasby, D. Turner, and L. Ackerman, "Matching of tomographic slices for interpolation," *IEEE Trans. Med. Imaging*, vol. 11, no. 4, pp. 507–516, 1992.

[52] J. Leng, G. Xu, and Y. Zhang, "Medical image interpolation based on multi-resolution registration," *Comput. Math. with Appl.*, vol. 66, no. 1, pp. 1–18, 2013.

[53] A. Horváth, S. Pezold, M. Weigel, K. Parmar, and P. Cattin, "High order slice interpolation for medical images," in *Simulation and Synthesis in Medical Imaging*, ser. Lecture Notes in Computer Science, S. Tsaftaris, A. Gooya, A. Frangi, and J. Prince, Eds., vol. 10557. Cham, Switzerland: Springer International Publishing, 2017, pp. 69–78.

[54] G. Penney, J. Schnabel, D. Rueckert, M. Viergever, and W. Niessen, "Registration-based interpolation," *IEEE Trans. Med. Imaging*, vol. 23, no. 7, pp. 922–926, 2004.

[55] G. Grevera and J. Udupa, "An objective comparison of 3-D image interpolation methods," *IEEE Trans. Med. Imaging*, vol. 17, no. 4, pp. 642–652, 1998.

[56] S. Raya and J. Udupa, "Shape-based interpolation of multidimensional objects," *IEEE Trans. Med. Imaging*, vol. 9, no. 1, pp. 32–42, 1990.

[57] M. Joliot and B. Mazoyer, "Three-dimensional segmentation and interpolation of magnetic resonance brain images," *IEEE Trans. Med. Imaging*, vol. 12, no. 2, pp. 269–277, 1993.

[58] J. Ehrhardt, R. Werner, D. Säring, T. Frenzel, W. Lu, D. Low, and H. Handels, "An optical flow based method for improved reconstruction of 4D CT data sets acquired during free breathing," *Med. Phys.*, vol. 34, no. 2, pp. 21–711, 2007.

[59] R. Krishnamurthy, J. Woods, and P. Moulin, "Frame interpolation and bidirectional prediction of video using compactly-encoded optical flow fields and label fields," *IEEE Trans. Circuits Syst. Video Technol.*, vol. 9, no. 5, pp. 713–726, 1997.

[60] B. Choi, J. Han, C. Kim, and S. Ko, "Motion-compensated frame interpolation using bilateral motion estimation and adaptive overlapped block motion compensation," *IEEE Trans. Circuits Syst. Video Technol.*, vol. 17, no. 4, pp. 407–416, 2007.

[61] S. Dikbas and Y. Altunbasak, "Novel true-motion estimation algorithm and its application to motion-compensated temporal frame interpolation," *IEEE Trans. Image Process.*, vol. 22, no. 8, pp. 2931–2945, 2013.

[62] B. Horn and B. Schunck, "Determining optical flow," *Artif. Intell.*, vol. 17, no. 1–3, pp. 185–203, 1981.

[63] S. Ertuk, "Perspective to block motion estimation for video compression: High-frequency component matching," *IEEE Signal Process. Lett.*, vol. 14, no. 2, pp. 113–116, 2007.

[64] A. Puri, H. Hang, and D. Schilling, "An efficient block-matching algorithm for motion-compensated coding," in *Proc. IEEE International Conference on Acoustics, Speech, and Signal Processing*, 1987, pp. 1063–1066.

[65] R. Young and N. Kingsbury, "Frequency-domain motion estimation using a complex lapped transform," *IEEE Trans. Image Process.*, vol. 2, no. 1, pp. 2–17, 1993.

[66] M. Pingault and D. Pellerin, "Motion estimation of transparent objects in the frequency domain," *Signal Process.*, vol. 84, no. 4, pp. 709–719, 2004.

[67] A. Huang and T. Nguyen, "A multistage motion vector processing method for motion-compensated frame interpolation," *IEEE Trans. Image Process.*, vol. 17, no. 5, pp. 694–708, 2008.

[68] W. Fernando, L. Udawatta, and P. Pathirana, "Identification of moving obstacles with pyramidal lucas kanade optical flow and k means clustering," in *2007 Third International Conference on Information and Automation for Sustainability*. IEEE, 2007, pp. 111–117.

[69] L. Y. Siong, S. S. Mokri, A. Hussain, N. Ibrahim, and M. M. Mustafa, "Motion detection using lucas kanade algorithm and application enhancement," in *2009 International Conference on Electrical Engineering and Informatics*, vol. 2. IEEE, 2009, pp. 537–542.

[70] G. Farnebäck, "Two-frame motion estimation based on polynomial expansion," in *Scandinavian conference on Image analysis*. Springer, 2003, pp. 363–370.

[71] F. Bartolini and A. Piva, "Median based relaxation of smoothness constraints in optic flow computation," *Pattern Recognit. Lett.*, vol. 18, no. 7, pp. 649–655, 1997.

[72] L. Alparone, M. Barni, F. Bartolini, and R. Caldelli, "Regularization of optic flow estimates by means of weighted vector median filtering," *IEEE Trans. Image Process.*, vol. 8, no. 10, pp. 1462–1467, 1999.

[73] L. Alparone, M. Barni, F. Bartolini, and V. Cappellini, "Adaptively weighted vector-median filters for motion-fields smoothing," in *Proc. IEEE International Conference on Acoustics, Speech, and Signal Processing*, vol. 4, 1996, pp. 2267–2270.

[74] G. Nielson, "Scattered data modeling," *IEEE Comput. Graph. Appl.*, vol. 13, no. 1, pp. 60–70, 1993.

[75] S. Cuomo, A. Galletti, G. Giunta, and L. Marcellino, "A novel triangle-based method for scattered data interpolation," *Appl. Math. Sci.*, vol. 8, no. 133–136, pp. 6717–6724, 2014.

[76] M. Smolik and V. Skala, "Large scattered data interpolation with radial basis functions and space subdivision," *Integr. Comput.-Aided Eng.*, vol. 25, no. 11, pp. 1–14, 2017.

[77] I. Amidror, "Scattered data interpolation methods for electronic imaging systems: A survey," *J. Electron. Imaging*, vol. 11, no. 2, pp. 157–176, 2002.

[78] C. L. Lawson, "Software for c1 surface interpolation," in *Mathematical software*. Elsevier, 1977, pp. 161–194.

[79] Z. Ma, J. Tavares, R. Jorge, and T. Mascarenhas, "A review of algorithms for medical image segmentation and their applications to the female pelvic cavity," *Comput. Methods Biomech. Biomed. Eng.*, vol. 13, no. 2, pp. 235–246, 2010.

[80] N. Sharma and L. Aggarwal, "Automated medical image segmentation techniques," *J. Med. Phys.*, vol. 35, no. 4, pp. 3–14, 2010.

[81] T. Bucking, E. Hill, J. Robertson, E. Maneas, A. Plumb, and D. Nikitichev, "From medical imaging data to 3D printed anatomical models," *PLoS ONE*, vol. 12, no. 5, pp. 1–10, 2017.

[82] F. Rengier, A. Mehndiratta, H. von Tengg-Kobligk, C. Zechmannand, R. Unterhinninghofen, H.-U. Kauczor, and F. Giesel, "3D printing based on imaging data: Review of medical applications," *Int. J. Comput. Assist. Radiol. Surg.*, vol. 5, no. 4, pp. 335–341, 2010.

[83] A. P. James and B. V. Dasarathy, "Medical image fusion: A survey of the state of the art," *Inf. Fusion*, vol. 19, pp. 4–19, 2014.

[84] R. Singh and A. Khare, "Fusion of multimodal medical images using daubechies complex wavelet transform–a multiresolution approach," *Inf. Fusion*, vol. 19, pp. 49–60, 2014.

[85] G. Bhatnagar, Q. J. Wu, and Z. Liu, "Directive contrast based multimodal medical image fusion in nsct domain," *IEEE Trans. Multimedia*, vol. 15, no. 5, pp. 1014–1024, 2013.

[86] M. Brock, B. Löppenberg, F. Roghmann, A. Pelzer, M. Dickmann, W. Becker, P. Martin-Seidel, F. Sommerer, L. Schenk, R. J. Palisaar *et al.*, "Impact of real-time elastography on magnetic resonance imaging/ultrasound fusion guided biopsy in patients with prior negative prostate biopsies," *J. Urol.*, vol. 193, no. 4, pp. 1191–1197, 2015.

[87] M. Brock, F. Roghmann, C. Sonntag, F. Sommerer, Z. Tian, B. Loppenberg, R. Palisaar, J. Noldus, J. Hanske, and C. von Bodman, "Fusion of magnetic resonance imaging and real-time elastography to visualize prostate cancer: a prospective analysis using whole mount sections after radical prostatectomy," *Ultraschall Med.*, vol. 36, pp. 355–361, 2015.

[88] S. S. Mahdavi, M. Moradi, W. J. Morris, S. L. Goldenberg, and S. E. Salcudean, "Fusion of ultrasound b-mode and vibro-elastography images for automatic 3-d segmentation of the prostate," *IEEE Trans. Med. Imaging*, vol. 31, no. 11, pp. 2073–2082, 2012.

[89] R. A. Schowengerdt, *Remote Sensing: Models and Methods for Image Processing*, 2nd ed. Orlando, FL, USA: Academic Press, 1997.

[90] T. Stathaki, *Image Fusion: Algorithms and Applications.* USA: Academic Press/Elsevier, 2008.

[91] L. Alparone, B. Aiazzi, S. Baronti, and A. Garzelli, *Remote Sensing Image Fusion.* Boca Raton, FL, USA: CRC Press, 2015.

[92] D. Jiang, D. Zhuang, Y. Huang, and J. Fu, "Survey of multispectral image fusion techniques in remote sensing applications," *Image fusion and its applications*, pp. 1–23, 2011.

[93] D. Bulanon, T. Burks, and V. Alchanatis, "Image fusion of visible and thermal images for fruit detection," *Biosyst. Eng.*, vol. 103, no. 1, pp. 12–22, 2009.

[94] L. Alparone, A. Garzelli, and G. Vivone, "Intersensor statistical matching for pansharpening: Theoretical issues and practical solutions," *IEEE Trans. Geosci. Remote Sens.*, vol. 55, no. 8, pp. 4682–4695, Aug. 2017.

[95] K. Hoffman and R. Kunze, "Linear algebra."

[96] C. A. Laben and B. V. Brower, "Process for enhancing the spatial resolution of multispectral imagery using pan-sharpening," 2000, U.S. Patent # 6,011,875.

[97] G. Vivone, L. Alparone, J. Chanussot, M. Dalla Mura, A. Garzelli, R. Restaino, G. Licciardi, and L. Wald, "A critical comparison among pansharpening algorithms," *IEEE Trans. Geosci. Remote Sens.*, vol. 53, no. 5, pp. 2565–2586, May 2015.

[98] J. Ma, C. Chen, C. Li, and J. Huang, "Infrared and visible image fusion via gradient transfer and total variation minimization," *Inf. Fusion*, vol. 31, pp. 100–109, 2016.

[99] L. Wald, *Data Fusion: Definitions and Architectures — Fusion of images of different spatial resolutions*. Paris, France: Les Presses de l'École des Mines, 2002.

[100] L. Wald, T. Ranchin, and M. Mangolini, "Fusion of satellite images of different spatial resolutions: Assessing the quality of resulting images," *Photogramm. Eng. Remote Sens.*, vol. 63, no. 6, pp. 691–699, Jun. 1997.

[101] C. Thomas and L. Wald, "Analysis of changes in quality assessment with scale," in *Proc. 9th Int. Conf. Inf. Fusion*, 2006, pp. 1–5.

[102] F. Palsson, J. R. Sveinsson, M. O. Ulfarsson, and J. A. Benediktsson, "Quantitative quality evaluation of pansharpened imagery: Consistency versus synthesis," *IEEE Trans. Geosci. Remote Sens.*, vol. 54, no. 3, pp. 1247–1259, Mar. 2016.

[103] L. Alparone, B. Aiazzi, S. Baronti, A. Garzelli, F. Nencini, and M. Selva, "Multispectral and panchromatic data fusion assessment without reference," *Photogramm. Eng. Remote Sens.*, vol. 74, no. 2, pp. 193–200, Feb. 2008.

[104] Z. Wang and A. C. Bovik, "A universal image quality index," *IEEE Signal Process. Lett.*, vol. 9, no. 3, pp. 81–84, Mar. 2002.

[105] M. M. Khan, L. Alparone, and J. Chanussot, "Pansharpening quality assessment using the modulation transfer functions of instruments," *IEEE Trans. Geosci. Remote Sens.*, vol. 47, no. 11, pp. 3880–3891, Nov. 2009.

[106] B. Aiazzi, L. Alparone, S. Baronti, R. Carlà, A. Garzelli, and L. Santurri, "Full scale assessment of pansharpening methods and data products," in *Proc. SPIE Image Signal Process. Remote Sens. XX*, L. Bruzzone, Ed., vol. 9244, 2014, pp. 924 402–1–924 402–12.

[107] L. Alparone, B. Aiazzi, S. Baronti, and A. Garzelli, "Spatial methods for multispectral pansharpening: Multiresolution analysis demystified," *IEEE Trans. Geosci. Remote Sens.*, vol. 54, no. 5, pp. 2563–2576, May 2016.

[108] J. Núñez, X. Otazu, O. Fors, A. Prades, V. Palà, and R. Arbiol, "Multiresolution-based image fusion with additive wavelet decomposition," *IEEE Trans. Geosci. Remote Sens.*, vol. 37, no. 3, pp. 1204–1211, May 1999.